3D Printing PTFE with Direct Ink Writing

by

Danny Zhuoran Jiang

A dissertation submitted to Johns Hopkins University in conformity
with the requirements for the degree of Master

Baltimore, Maryland

July, 2018

Abstract

Polytetrafluoroethylene (PTFE) is a unique fluoropolymer comprising of only fluorine and carbon atoms with various desirable properties such as non-stick, chemical inertness, thermal stability and electrical insulation. Molding and sintering techniques following by pressurized preforming are commonly used to cast PTFE for desirable shapes and forms with considerable amount of waste under high cost. However, rapid prototyping and customizable tooling of PTFE is yet developed. Herein, we reported a novel and facile way for PTFE 3D printing by Direct Ink Writing (DIW). PTFE dispersion based composite, with varying amount of Gellan gum additives, was developed as 3D printable ink to generate millimeter features following by multi-steps thermal process. In order to fabricate molding PTFE properties similar structures, the design of experiments (DOE) method based on Taguchi's orthogonal arrays were applied. The printed structures were prepared by varying three controlled factors including the Gellan gum weight percentage, the maximum temperature, and the cooling rate with three selected levels. An optimal parameter setting is obtained through a desirability function analysis of variance (ANOVA) that balances the desired Young's modulus and yield strength targets. The Young's modulus and yield strength are found to be controllable by varying the amount of Gellan gum. Based on its mechanical, hydrophobic and chemical inert properties, tubular structures with various designs were fabricated to demonstrate its potential in medical implants.

Advisor: David Gracias

Reader: Anirudha Singh

Zhuoran Jiang, Devina Chatterjee, Ozan Erol, Weinan Xu, Narutoshi Hibino, Lewis Romer, Sung Hoon Kang, and David H. Gracias. 3D Printing PTFE with Direct Ink Writing. *In preparation.*

Acknowledgements

I would like to genuinely thank Prof. Gracias for his support and guidance through my research and study during these two years at Johns Hopkins University. I will not be able to understand and undergo how research is performed from an idea to a done project without the opportunity to work in Gracias' Lab. I express my sincere appreciation to the National Institute of Health (NIH), United States, for financial support under project number: 1R21HD090663-01.

I would like to sincerely express my gratitude to the CO-PI of this project Prof. Kang for his inspiring suggestion and concerns when my research work came to a standstill. I would also like to thank Prof. Singh to my thesis reader and suggestion through the writing process. In addition, I would like to thank Prof. Pereira for being part of his wonderful chemical engineering class as both a student and a grader.

I sincerely appreciate every help from my dearest and best lab collaborator ever: Dr. Ozan and Devina for their efforts and input from the start of this project. This work would not have been possibly done without both of you. I feel grateful to work with Kuniniko Kobayashi that his guidance and his knowledge of polymers inspire me to develop my own independent research project. I would like to especially thank Dr. Xu and Dr. Chen from Gracias' Lab providing a lot of knowledge and discussion in the material characterization part. Everyone in our lab is accommodating when helps are needed.

Lastly, I would like to sincerely thank my parents for supporting my financially and mentally for any decisions I made in my life.

Table of Contents

List of Figures

List of Tables

1. PTFE and its fabrication

1.1 Introduction

1.1.1 Polytetrafluoroethylene (PTFE)

Polytetrafluoroethylene (PTFE) is a fluorinated polymer with many desirable properties produced by the polymerization of tetrafluoroethylene. It is now known by DuPont's trademark as Teflon®. PTFE is distinguished by its low coefficient of friction, high melting point, and resistance to attack by almost all chemicals. These properties have made it familiar to consumers as the coating on nonstick cookware. Other well-known applications include piezoelectric systems, biomedical implants and devices, and mechanical joints, gaskets in chemical processes [1-3].

PTFE was discovered serendipitously by Roy Plunkett, a DuPont Company chemist in 1938, who found that a tank of gaseous tetrafluoroethylene refrigerant had polymerized to a white powder. Due to the natural properties of PTFE, i.e. low friction coefficient and high melting viscosity, PTFE found to be non-machine manufactural and saw little commercial use for more than a decade after the World War II. DuPont released its trademarked Teflon-coated nonstick cookware in early 1960.[1,4-6]

In a chemistry viewpoint, tetrafluoroethylene (C_2F_4) is a colourless and odourless gas which is made by heating chlorodifluoromethane ($CHClF_2$) in the range of 600–700 °C or 1,100–1,300 °F.[7] The product of the reaction between hydrogen fluoride (HF) and chloroform ($CHCl_3$) is chlorodifluoromethane ($CHClF_2$). Emulsification of tetrafluoroethylene (C_2F_4) monomers in water following by polymerization under high pressure in the presence of free-radical initiators is an industrial standardized procedure. The polymer consists of a chain of carbon atoms with two fluorine atoms bonded to each carbon shown in Figure 1.

Fluorine (F) has highest electronegativity among all elements and it is highly reactive, where the electronegativity of Carbon (C) is significantly lower than Fluorine. Resulting to high electron density, and thus polarity, where the unshared electron pair is pulled towards F from C. The compact interlocking of Fluorine atoms alongside stronger and stable $C-F$ bonds are the reasons for high heat stability where its melting point is around 327°C.[8] Fluorine atoms tends to be negatively charged and expected to have higher intra-molecular and intermolecular forces due to the electron affinity. However, PTFE is electronically neutral due to the cancelation of the dipole moments of neighboring symmetrical structures. And consequently, this physical phenomenon leads to a low coefficient of friction.[9]

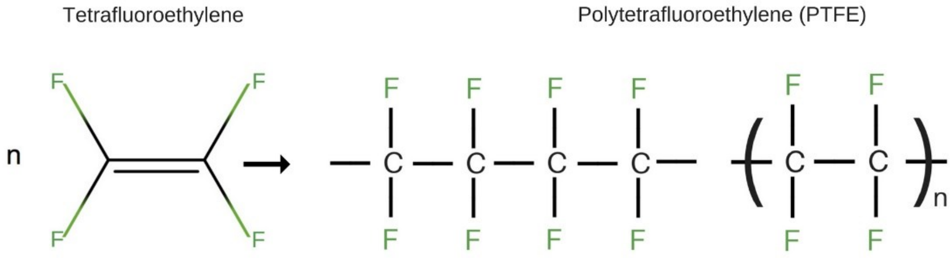

Figure 1. Schematic diagram of Polytetrafluoroethylene (PTFE) chemical structure

1.1.2 PTFE product fabrication process by molding and sintering

Even though PTFE is a thermoplastic, it cannot be processed using conventional polymer processing techniques due to its high melting viscosity. Thus, cold shaping operation following by heat treatment, named sintering, during which polymer particles fuse to form a solid molding is used in the industry. Molded parts can be made by compressing and heating fine powders mixed with volatile lubricants.[10] Metallic surfaces can be sprayed or dipped with aqueous dispersions of PTFE particles to form a permanent coating.[11] Dispersions of PTFE can also be spun into fibers.[12]

Currently, there are three primary ways to commercially manufacture PTFE: compression molding, paste extrusion, and isostatic molding. The most common way of processing PTFE is compression molding by extrusion as shown in Figure 2 as below.[13] The PTFE powder resin is made with suspension polymerization to produce granular molding resins. It is then compressed under high pressure of around 30 MPa and then sintering to a high temp 340-400 degrees C.[14] But this molding process can be used only for a limited type of structures. For advanced and complex structures, isostatic molding is performed. In this advanced process a rubber mold of the desired structure is made and is filled with PTFE. Then the mold is placed into a high pressure chamber where the mold in compressed, and thus compressing the PTFE into the structure.[1,14,15] The equipment needed to process PTFE are high in price and the process of molding PTFE produces lot of scraps of excess PTFE which cannot be recycled. Thus these molding processing methods result in higher price and low customization for PTFE structures.

Sintering following by molding is typically used in PTFE fabrication. Sintering a PTFE molding involves heating it at a temperature well above its crystalline melting point of about 340 degrees C until the individual PTFE particles coalesce and lose their identity. The melting point falls to the traditionally quoted 327 degrees C only after PTFE has been melted for the first time. Design of sintering cycle follows careful investigation of the following parameters: the maximum temperature, the rate of heating, the rate of cooling and the section thickness of PTFE samples.

In order to have faster, therefore more productive, sintering process, higher maximum sintering temperatures are often chosen. However, an upper limit is imposed by the tendency of PTFE to degrade slightly at very high temperatures. Small molding parts can endure slightly higher temperature in general. However, for thicker molding structures and fillers containing PTFE composites, which meaning less thermal stabilities comparing to pure PTFE parts, it is advisable to reduce the peak temperature to 360°C. Sintering can happen as long as temperature go beyond the melting point, therefore, the effective sintering time is always longer than the dwell period at maximum temperature.

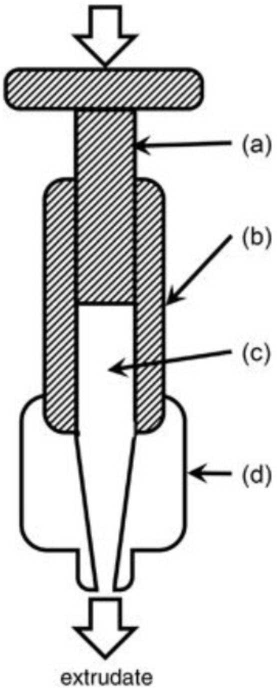

Figure 2. Schematic diagram of typical industrial manufacturing process by extrusion molding: a) ram, b) cylinder, c) PTFE mixture, and d) die. Reprinted permission from[13]. Copyright © Springer Nature

The initial heating rate of sintering is limited by the need to minimize stresses set up in the molding as it expands on temperature near the melting point. 20% to 25% is a typical volume expansion value during the heat up process from solid to gel state. Thin section moldings can be treated with a fast ramping rate as fast as the heating equipment can go up to, or even to place the molding in an oven already heated to 380°C. However, a dwell period around PTFE's maximum service temperature, 260 to 310°C, is often used for thicker molding sections. The reason behind is to make sure the entire molding reaches the same temperature before it passes into the gel state.

Lastly, the quenching rate as the final step of sintering cycle is also one of the essential parameters to control. The rate of cooling is governed mainly by the crystallinity required in the finished product, slow cooling giving maximum crystallinity, and quench cooling minimum crystallinity. Similarly, fast cooling rate can be considered for thin molding parts to increase productivity. For thicker moldings, slow cooling is advised as the risk of introducing high stresses which may cause cracking or severe distortion. In general, slow cooling rate from the maximum temperature to 300°C, followed by a dwell period is used to minimize residual stress inside the molding parts. 6 hours dwell time at around 250°C is used if one required completely stress-free moldings. In the end, a slow cooling rate not greater than 30°C/hour is usually used to let the product further cool down to room temperature.[1]

Table 1 shows a typical industrial thermal processing cycle for PTFE moldings. Seven intervals with three dwell periods in heat-up, melting, and quenching are included. The length of each intervals is governed by the section thickness of the molding. Theoretically, the thickness is defined as the minimum dimension of wall thickness of a tube, the diameter of a solid rod, or the thickness of a sheet or disc. Figures 3 shows the graph of a complete cycle for molding parts regardless of thickness of the structure. Specifically, the thickness range of 20 - 50 mm of molding parts are relatively negligible as regards to the sintering cycle. However, as sintering time and temperature can have a marked effect on the end properties of PTFE moldings. Once a specific sintering cycles is chosen, it must be consistently used regardless of the dimensions of the rest products if moldings of consistent quality are to be produced.

Interval Number	Temperature range (°C)	Time (Hr)
1	R.T. to 310	7
2	Dwell at 310	0
3	310 to 380	4
4	Dwell at 380	5.5
5	380 to 300	4
6	Dwell at 300	0
7	300 to 100	4.5

Table 1. Typical thermal steps in PTFE industrial sintering cycle.

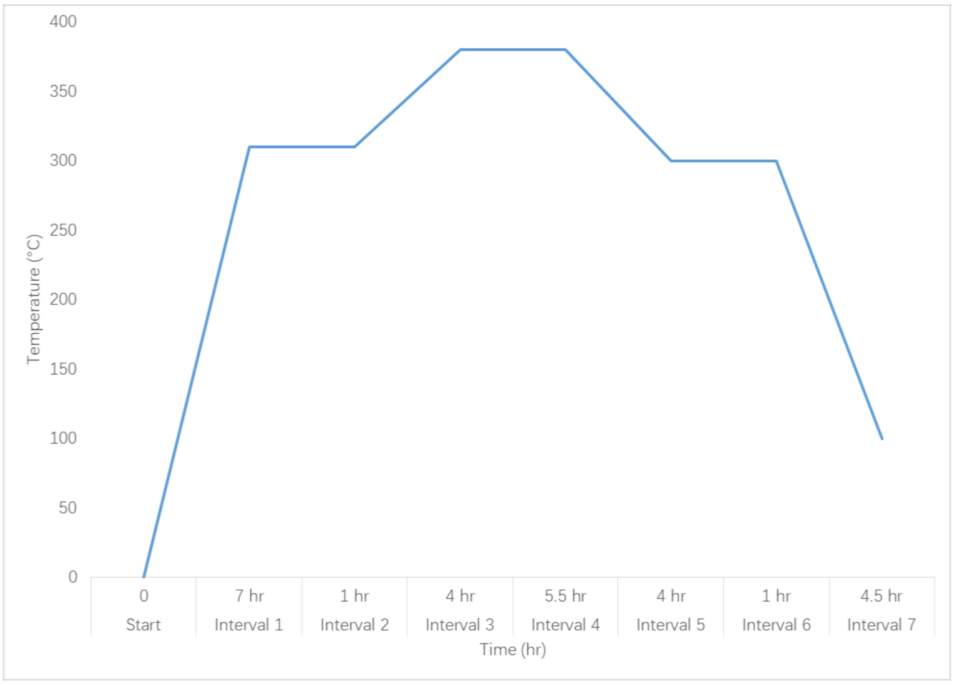

Figure 3. Typical thermal steps in PTFE industrial sintering cycle.

1.1.3 PTFE 3D Printing

The 3M Company claimed that they are able to able to 3D print PTFE with 3M™ Dyneon™ PTFE successfully. Stereolithography, known as SLA, was used for 3D printed PTFE. SLA is a technique that converts liquid materials in resin form into solid parts layer by layer. Curing of liquid resin is done by using a light source selectively in a process called photopolymerization. SLA is widely used to create models, prototypes, patterns, and production parts for a range of industries from engineering and product design to manufacturing as shown in Figure 4.[16]

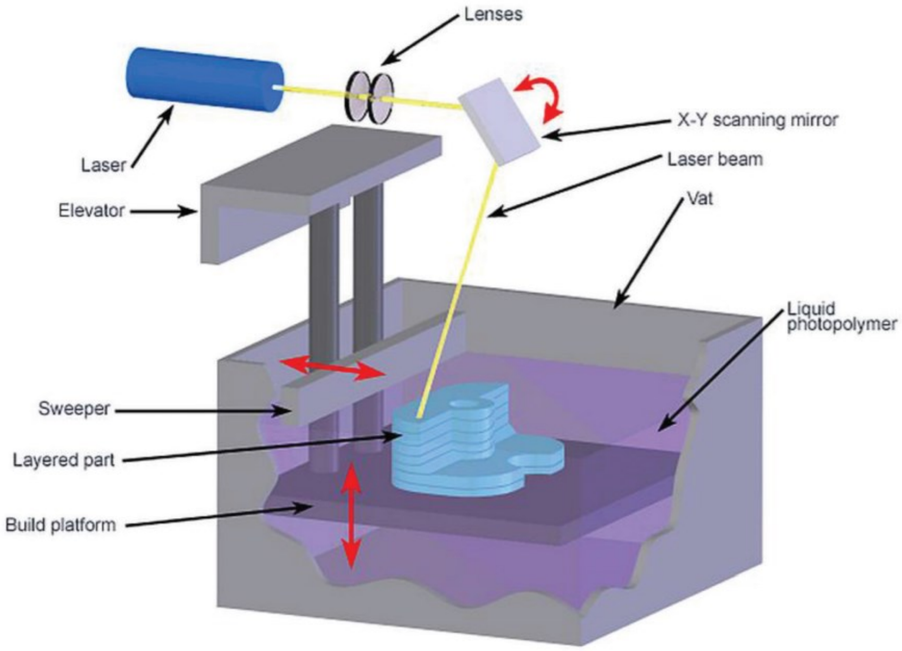

Figure 4. Schematic diagram of SLA 3D printing technique. Preprint permission from[16]. Copyright © 2018 The Author(s). Licensee InTech.

In this process a precisely controlled, high power laser is used to crosslink the resin layer by layer. While the method is efficient in making printed structures considering the amount of wasted resin. So far, the available properties of printed PTFE are its yield strength, ranges from 8 to 12 MPa with 10% offset under ASTM D1708, and a smoother surface shown by dome-shaped printed features without any quantification. Furthermore, patents regards to 3M 3D printing with 3M™ Dyneon™ PTFE are still suspending. No patents are released from 3M Company yet thus far.

1.1.4 Direct Ink Writing 3D printing technique

Direct ink writing, known as DIW, is one of the 3D printing fabrication methods that employ a computer-controlled translation stage embedding with ink-deposition nozzle, which generates 3D patterns by extruding material from pre-loaded ink cartridges with controlled architecture and composition.[17]

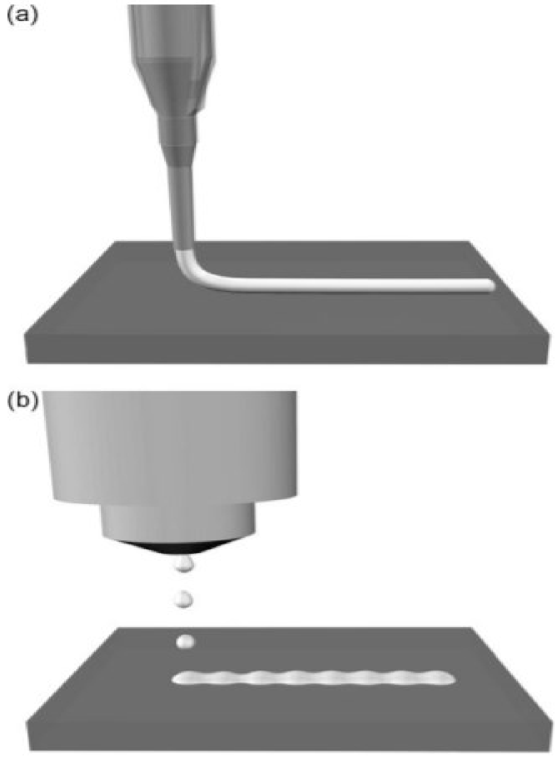

Figure 5. Schematic diagram of DIW; a) the filamentary-based DIW; b) the droplet-based DIW. Reprint permission from[18]. Copyright © John Wiley and Sons

DIW is a concept raised by Jennifer A. Lewis, where she further categorizes that the filamentary-based approaches and the droplet-based approaches are two basic type of DIW, as shown in Figure 5 a) and b).[18] The filamentary-based approaches includes robocasting,[19,20] micro-pen writing,[21] and fused deposition.[22] Such as ink-jet printing,[23] and hot-melt printing[24] are counted as the droplet-based approaches. One important part to make DIW successful is to make 3D printed ink as shear thinning materials. Strategies of transferring Newtonian fluids, including various gels and liquid solvent, are to use highly shear thinning colloidal suspensions,[21] colloidal gels,[25] polymer melts,[26] dilute colloidal fluids,[27] waxes,[28] and concentrated polyelectrolyte complexes as shear thinning agents or additives.[29] The solidification methods of above inks can be generally classified into liquid evaporation,[23] gelation,[30] or a temperature[31] or solvent-induced phase change.[32]

By controlling the ink composition and printing parameters, various 3D designs can be printed to construct for example continuous, spanning or high aspect ratio features. Self-spanning structures, especially latter structures, are one of the most challenging one to print due to the self-supporting parts underlying features that span gaps. Periodic architectures employing filamentary features with various sizes are one of the most interesting field raising in DIW 3D printing. Concentrated colloidal, fugitive organic, and polyelectrolyte inks are widely used to render such hierarchical architectures because of their respective applications such as functional composites,[33] microfluidic networks,[30] and templates for photonic bandgap materials[34] and inorganic–organic hybrid structures.[32]

1.1.5 Gellan Gum

Gellan gum was first approved for use in food industry in Japan around 1990. Each repeated unit of gellan gum consists of a tetra-saccharide unit, glucose, glucuronic acid, glucose and rhamnose, shown in Figure 6 a).[35,36] Transparent gel can be formed in the presence of divalent cations, such as Ca^{2+}.[37] It is well known that gellan gum exhibits a conformational change from the disordered state (single chain) to the ordered state (double helix) with decreasing temperature, and the gelation is considered to be mediated by the double-helix formation and the association of such helices which is enhanced by the presence of metallic cations.[37-39] Gellan gum hydrogel is a good example of thermos-reversible sol-gel transitions because it dissolves well in water if it is converted into, for example, a sodium type, and it forms a transparent gel. The structure of the gel network and the chain properties between crosslinks can affect the physical nature of the gel state. The temperature related rheological and physicochemical properties of gellan gum coiling mechanism in the sol-gel transition state attracts many research interests. [40-43]

The mechanism of gellan gum gelation is now well deduced largely from physical and physical-chemical studies.[44] Oriented gellan gum fibers produce excellent X-ray diffraction patterns.[45] Analysis of these patterns has led to atomic resolution models for gellan helices and their packing within the crystalline junction zones formed in the presence of certain gel-promoting cations.[46] Therefore, due to the binding of certain cations, locally aggregated regions or so called physically crystalline regions are formed within the junction zones. Two separable and thermos-reversible steps are involved in the gelation process.[47,48] The first stage is a conformational change of the polysaccharide from a disordered coil form to an ordered helical structure, as shown in Figure 6 b)[48]. This ordered helical stage is also accompanied by intermolecular association or aggregation of the polysaccharide chains at sufficient

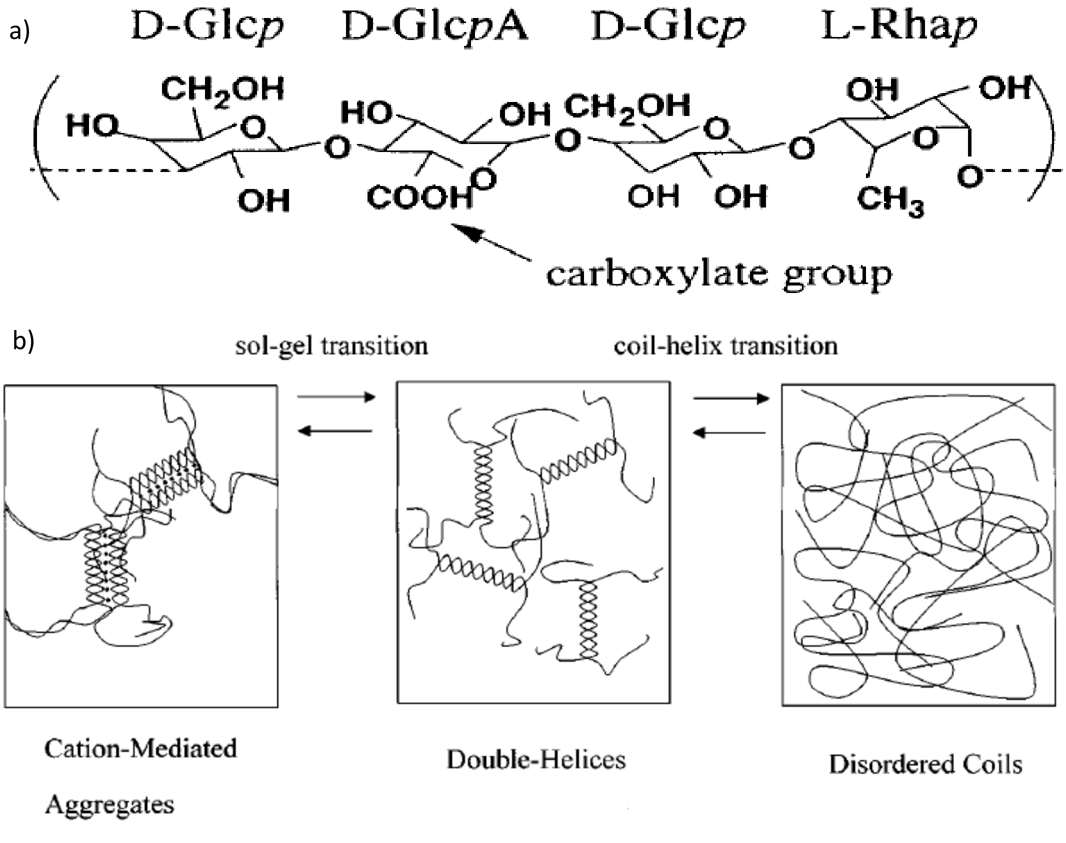

Figure 6. a) Chemical structure of gellan gum repeated unit;[36] b) Conformational change of gellan gum in sol-gel transition and coil-helix transition.[48] Reprinted permission from[36,48]. Copyright © Springer Nature.

high gum concentrations. In general, week gel-networks appear without the present of gel-promoting cations at concentration above the critical concentration for gelation; however, this network structure easily breaks under strain, resulting in a dispersion of aggregated structures. However, in the presence of gel-promoting cations the gel network structures formed above the critical concentration for gelation are permanent.[49] The cations are believed to facilitate and stabilize association of gellan helices by binding within the junction zones of the gel.

Gellan Gum hydrogel exhibits shear thinning properties at various temperature range. The temperature dependence of the storage modulus and the loss modulus are shown in Figure 7. In thermal scanning rheological measurement, two transitions of gellan gum solutions, the coil-helix transition and the sol-gel transition, respectively, were identified.[50] In concentrated solutions, where the number of aggregated helices exceeds a critical value on cooling, the rheological behavior changed from sol to gel. Furthermore, this sol-gel transition appeared as the crossover temperature of storage modulus and loss modulus. Both transition temperatures shifted to higher temperatures with increasing concentration of Gellan Gum.[51]

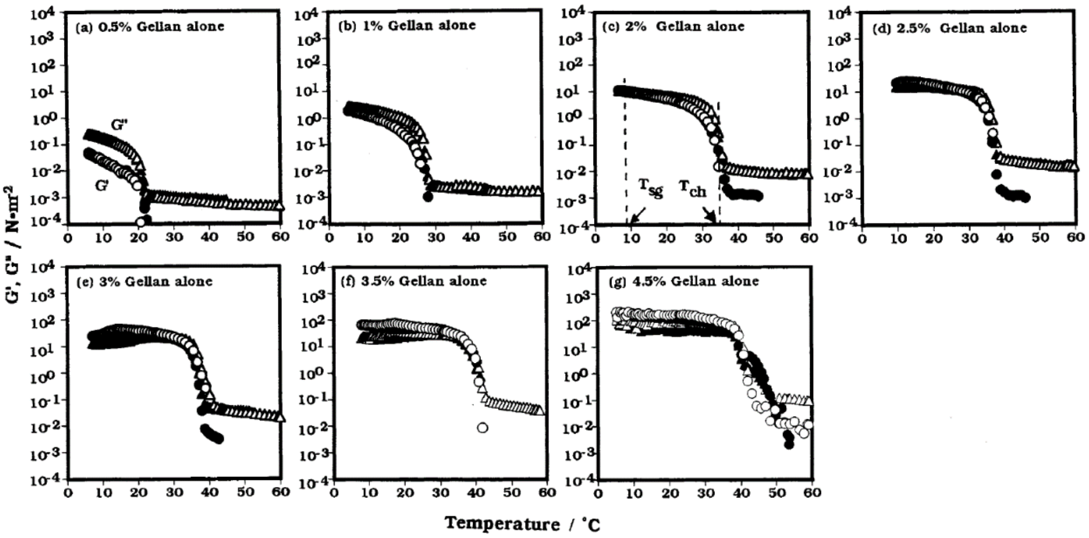

Figure 7. Shear thinning properties of gellan gum at various temperature range.[50] Reprinted permission from[50]. Copyright © Springer Nature.

1.2 Experimental Section

Materials: G1910 Gelzan Cm, Gellan Gum were obtained from Sigma–Aldrich. 665800 Polytetrafluoroethylene preparation 60% weight percentage dispersion was obtained from Sigma Aldrich. All materials were used as supplied.

DIW 3D-printing**:** The PTFE dispersion and Gelzan inks were initially loaded into a planetary/centrifugal mixer PE container. The components were mixed at 2000 RPM for 3 cycles of 30s each. The inks were then loaded into 3 mm Cellink syringe barrels and centrifuged at 1000 RPM for 1 min. The cartridges are then assembled to the Direct Ink Writing 3D Printer (Inkredible+ 3D Bioprinter, Cellink) and connected to air pump. Pressure of 5 to 170 Pa were used. The structures were printed with an 18 G (12.22 mm) nozzle. Files made with Solidworks were used to design and create the structures. The structures were printed on a Teflon sheet (McMaster-Carr), which aided in the release of the printed structure from the substrate after the freezing for 60 minutes at -27°C. The structures were then taken off the Teflon sheet and then taken to a 1700°C high-temperature atmospheric furnace and underwent different heat cycles

Ink Rheology: Rotational rheology measurements were performed on an Anton-Paar Instruments MCR-9 rheometer, using a 1° cone and plate setup. The temperature of the plate was kept at 23 °C. Ink viscosities were measured at shear rates ranging from 0.01 to 1000 s−1. Oscillatory measurements of the elastic and viscous moduli were performed at a constant frequency of 1 Hz.

Characterization: Thermal characterization includes the differential scanning calorimetry (DSC) and the thermogravimetric analysis (TGA). The DSC measurements were carried out using a TA Instruments Q20 for both PTFE dispersion and PTFE/GG composite. The TGA measurements were performed using the Perkin Elmer TGA 8000 at a scanning rate of 10°C/min from room temperature to 800°C under nitrogen flow. Scanning electron microscope (SEM) images were obtained using a JSM-IT100 SEM.

1.3 Results and discussion

1.3.1 PTFE 3D Printing process with DIW

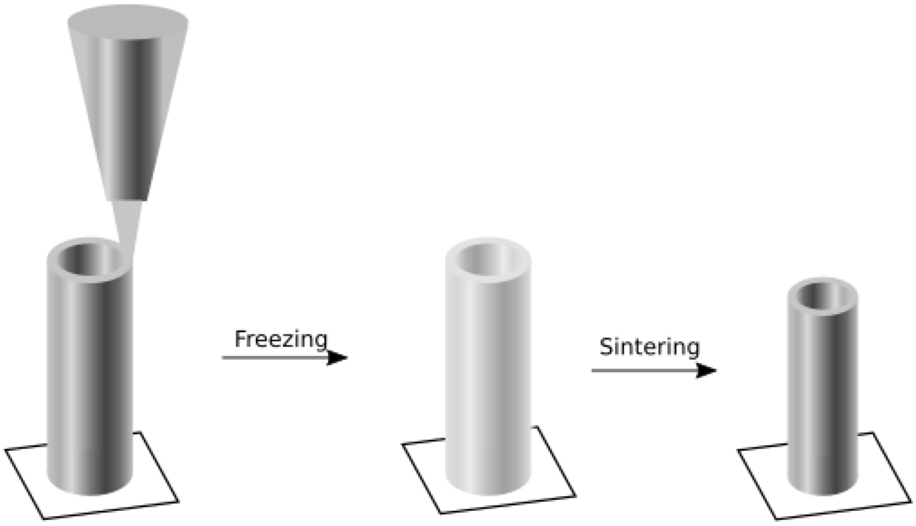

Figure 8. Schematic diagram of 3D printing PTFE by DIW with a tubular structure.

Various tubular designs were firstly drawn in 3D AutoCAD, and translated into modifiable STL files. Printer setting was adjusted with proper extrusion pressure and printing speed. Printing nozzle with outer diameter 1.2 mm was used consistently during the printing process. Glass slides with PTFE membrane taped on top were used as printing substrates. The tubular features were constructed by filament extrusion in a layer-by-layer manner. As-printed structures are brittle and easily break into parts due to the lack of mechanical properties. Freezing such structures in negative 80°C for 30 minutes gave as-printed structures stiffness to some extends due to water freezing. Then the solid structures were placed into high temperature atmosphere furnace for further sintering. Figure 8 shows a schematic diagram of the DIW 3D printing of PTFE process.

1.3.2 Printability Characterization

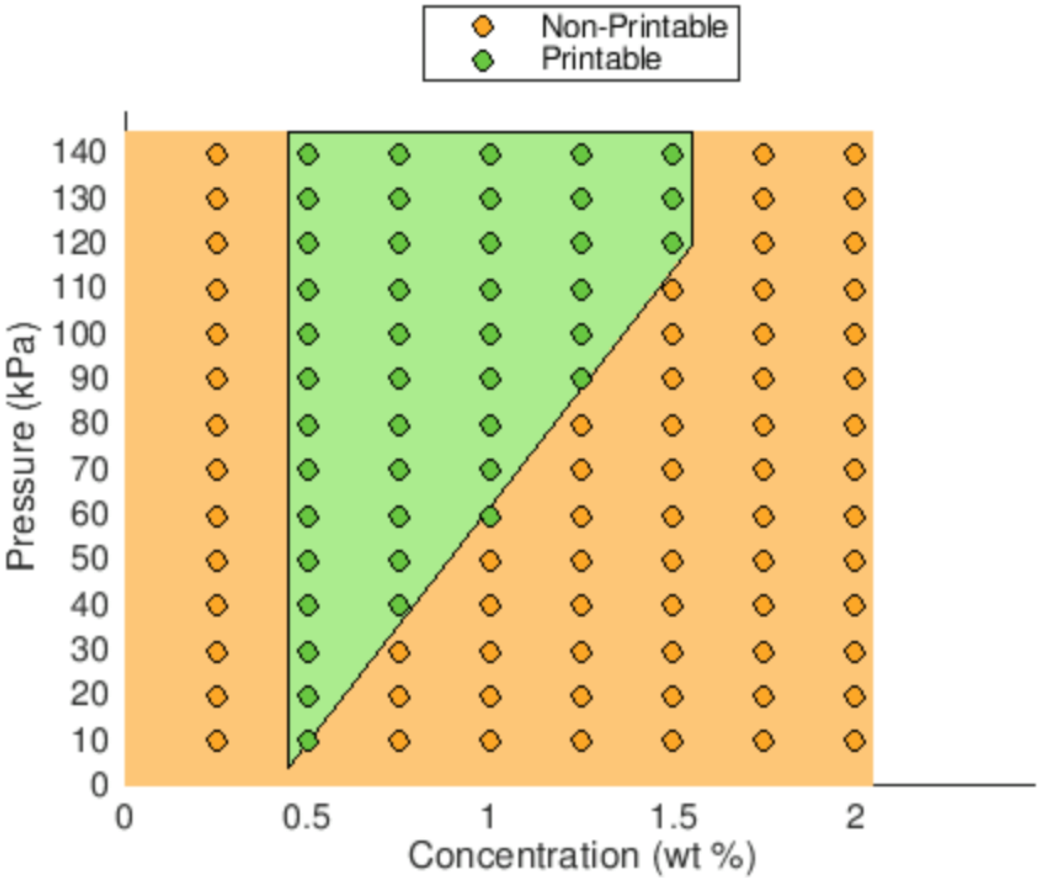

Figure 9. Printability graph indicating printable regions with known pressure at various gellan gum concentration.

The printability of the composite ink was evaluated by varying the printing pressure and gellan gum concentration in the ink, while fixing other parameters including nozzle diameter, and printing temperature. We found the ink can be printed into 3D structures when the concentration of gellan gum in the composite is between 0.5 and 1.5 wt% and the pressure is above a certain threshold, as shown in Figure 9. When gellan gum concentration is below 0.5 wt% or above 1.5 wt%, the ink cannot be printed due to liquid spreading or nozzle clogging, respectively; and when the printing pressure is below the threshold value, the ink cannot flow out of the nozzle.

a)

1.3.3 Ink Rheology Characterization

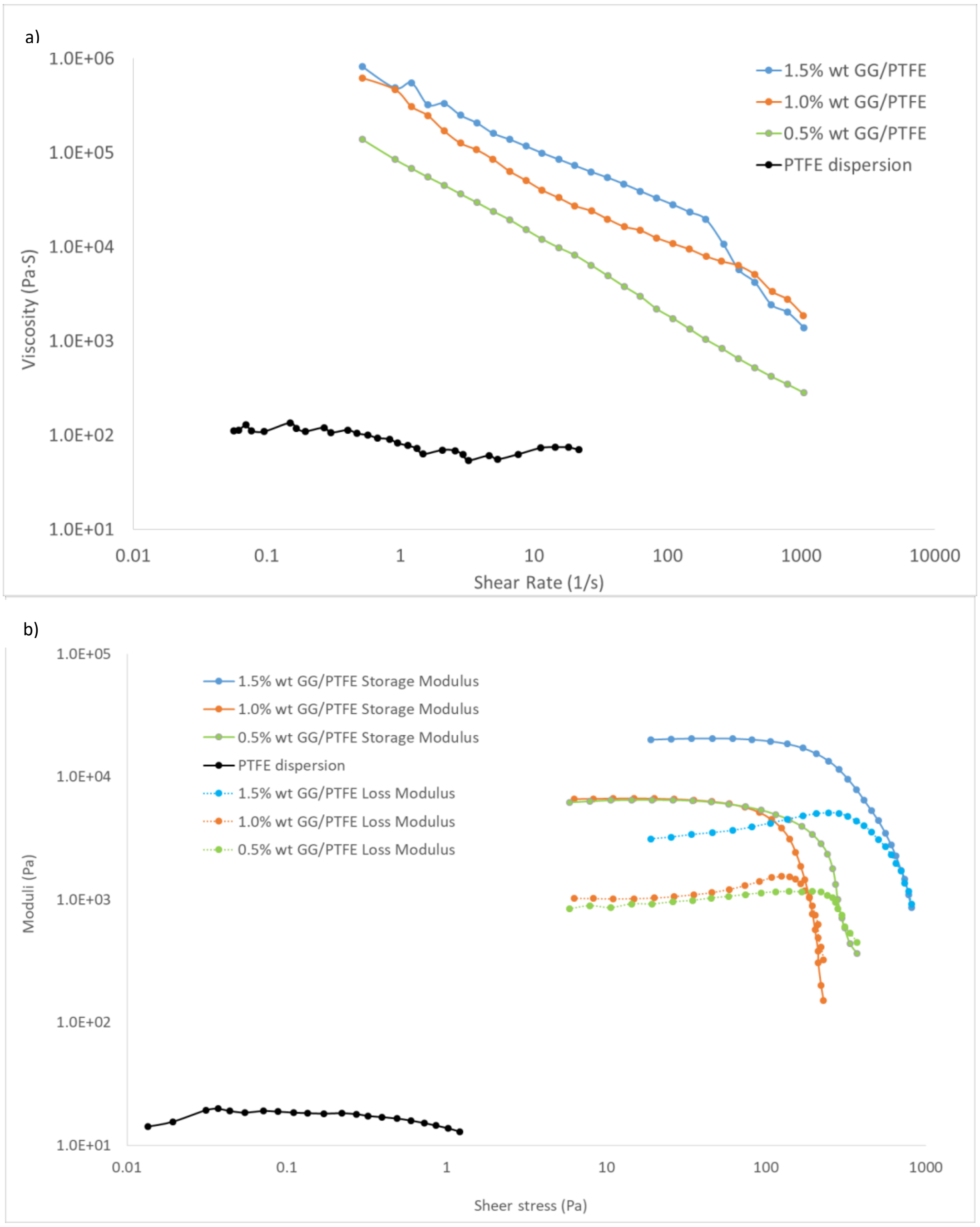

Figure 10. Rheology characterization of inks with various gallan gum concentration; a) Viscosity versus shear rate; b) Storage and loss modulus versus shear stress.

The rheological behavior of composite inks of varying composition are shown in Figure 10. The pure PTFE dispersion exhibits a viscosity around 100 Pa•s that is independent of shear rate as shown in Figure 10 a). As a consequence, the shear storage modulus of this ink is lower than its loss modulus, and both moduli are independent of applied shear stress as shown in Figure 10 b). While the PTFE dispersion readily flows through fine nozzles under modest applied pressures, it immediately wets and spreads upon exiting the nozzle and lacks the ability to support itself. The addition of Gellan Gum transforms the dispersion into a viscoelastic fluid. The resulting material, referred to as the composite ink, possesses a viscosity that exceeds 10^7 to 10^8 Pa•s at low shear rates (~0.01 s^{-1}) that is four orders of magnitude higher than the pure dispersion. Due to its strong shear thinning behavior, this ink exhibits an apparent viscosity of 10^4 to 10^5 Pa•s at shear rates (~50 s^{-1}) typically experienced during printing. Hence, the ink viscosity is two order of magnitude higher than that of the dispersion alone under relevant printing conditions. The composite ink exhibits a plateau value of storage modulus at around 10^4 Pa. With the increasing amount of gellan gum additives, the plateau modulus of each ink ranges from 10^4 to 20^4 Pa, while their shear yield stress ranges from 100 to 500 Pa, respectively. The decreasing trend of these key rheological parameters are in good agreement with the pressure enhancement in the printability characterization result.

1.3.4 Thermal process and thermal properties characterization

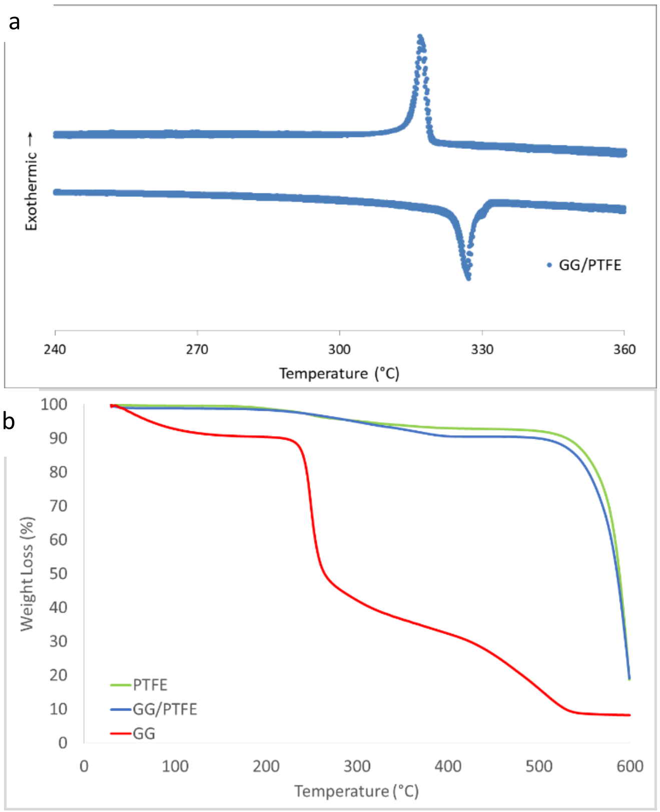

Figure 11. Thermal properties characterization of bulk PTFE dispersion and composite ink; a) TGA of PTFE, inks and gellan gum; b) DSC of PTFE and inks.

Sintering temperature plays an important role on the formation of 3D printed PTFE. DSC analysis (Figure 11 a) indicated that PTFE had a melting temperature of 327.4°C. TGA curves (Figure 11 b) showed that GG/PTFE ink started to decompose at around 470°C and the residual was less than 20 wt% at 600 C. GG/PTFE (1.5 wt%) composite fibers showed two weight-loss steps. The first weight loss (~10 wt%) occurred between 25–300°C, which was corresponding to the decomposition of gellan gum and the residual solvent from PTFE emulsion. The second weight loss started at 472.5 C, which was attributed to the decomposition of PTFE. In conclusion, the sintering temperatuDyre could be in the range of 330–430 C. To investigate the effect on mechanical properties, hydrophobicity and chemical resistance, sintering temperature and cooling rate with three different levels with varying gellan gum concentration were chosen for the treatment of GG/PTFE composite ink, as shown in Figure 12. A typical heating rate at 60°C/hr is chosen for the sintering cycle. In general, dwell periods at maximum service temperature (260°C) and maximum sintering temperature are key features for a typical sintering cycle, where the time of heat conduction are taking into account. We aimed to perform a fabrication recipe of novel 3D printed PTFE materials, therefore a Taguchi DOE was carried out with three parameters including maximum sintering temperature and cooling rate. The three levels of maximum sintering temperature are 340°C, 380°C and 420°C; and cooling rate are 12°C/hr, 60°C/hr and 150 °C/hr, respectively.

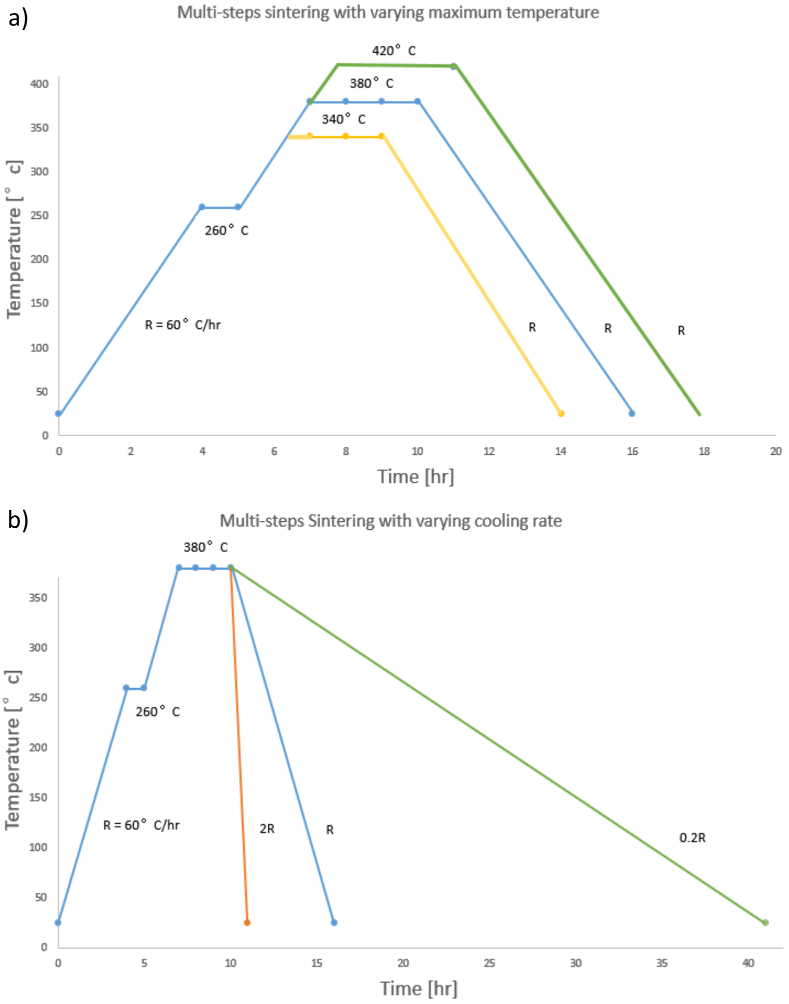

Figure 12. Sintering cycle with multiple thermal steps at a) different maximum temperature, and b) cooling rates.

1.3.5 Morphology studies

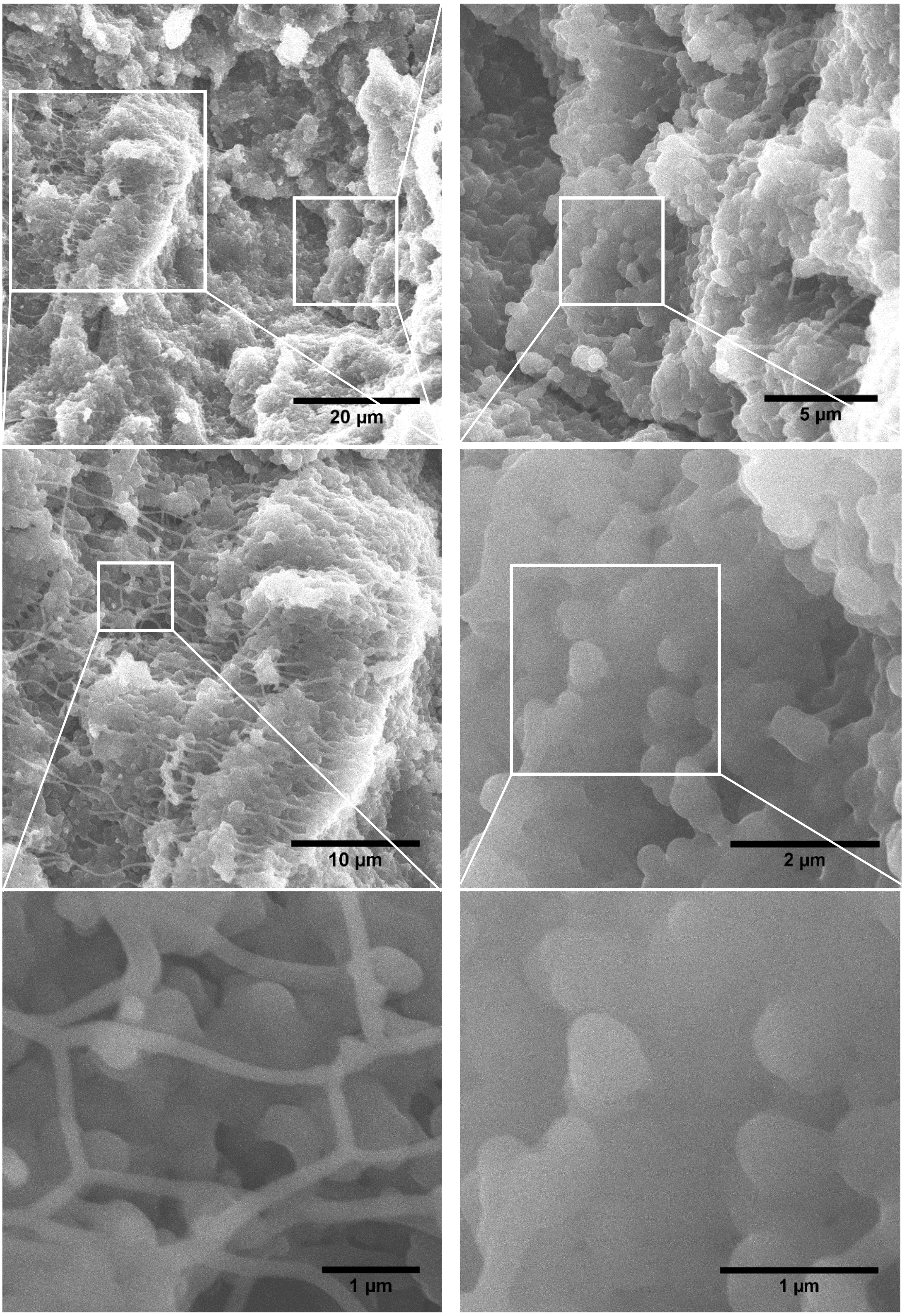

Figure 13. Scanning electronical microscope of ink composites after 3D printing； a) scale bar in 20 um; b) scale bar in 10 um; c) scale bar in 1 um; d) scale bar in 5 um; e) scale bar in 2 um; f) scale bar in 1 um.

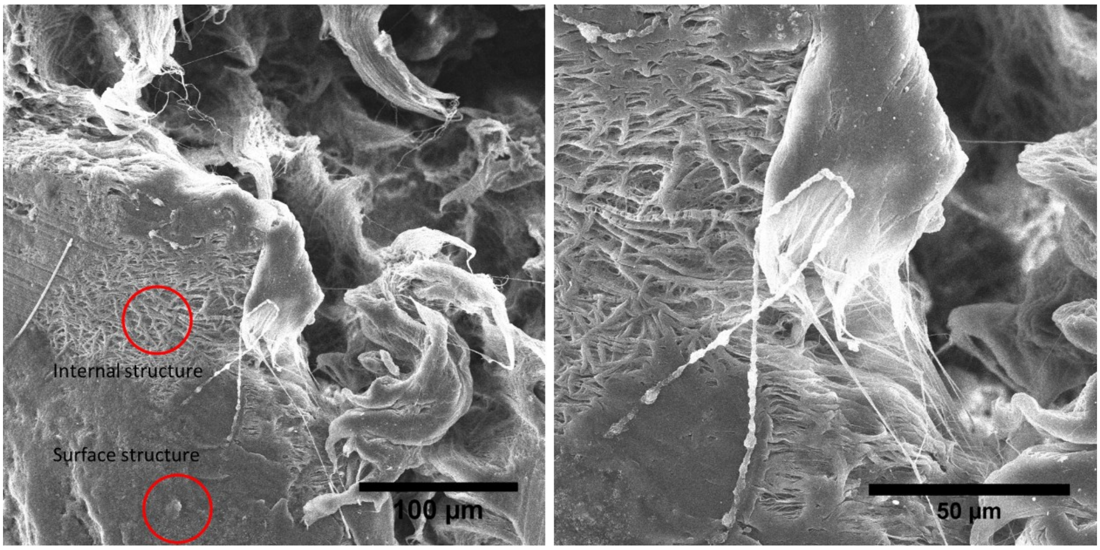

Figure 14. Scanning electronical microscope of ink composites after sintering；a) cycled for internal and external structures with scale bar in 100 um; b) scale bar in 50 um.

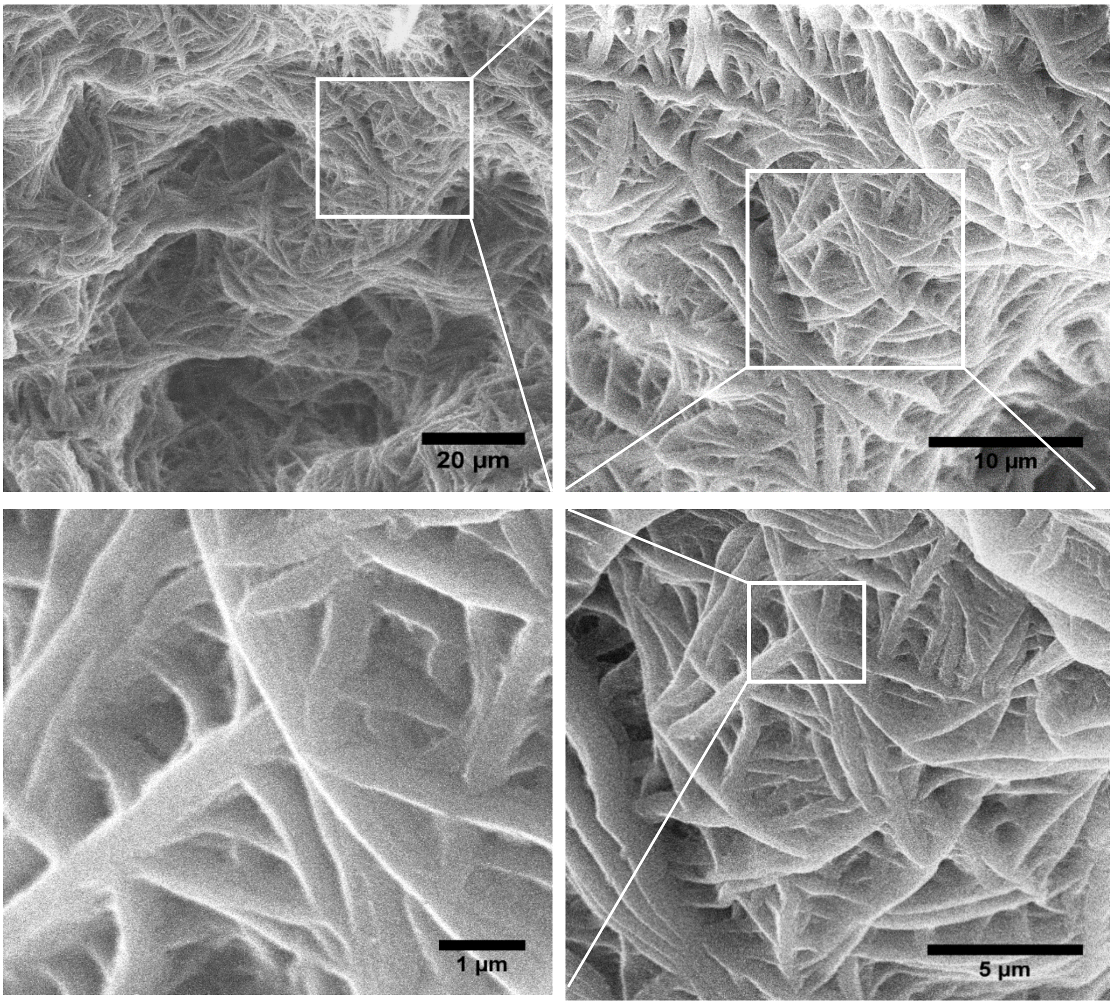

Figure 15. Scanning electronical microscope of composites inner structure after sintering；a) scale bar in 20 um; b) scale bar in 10 um; c) scale bar in 5 um; d) scale bar in 1 um.

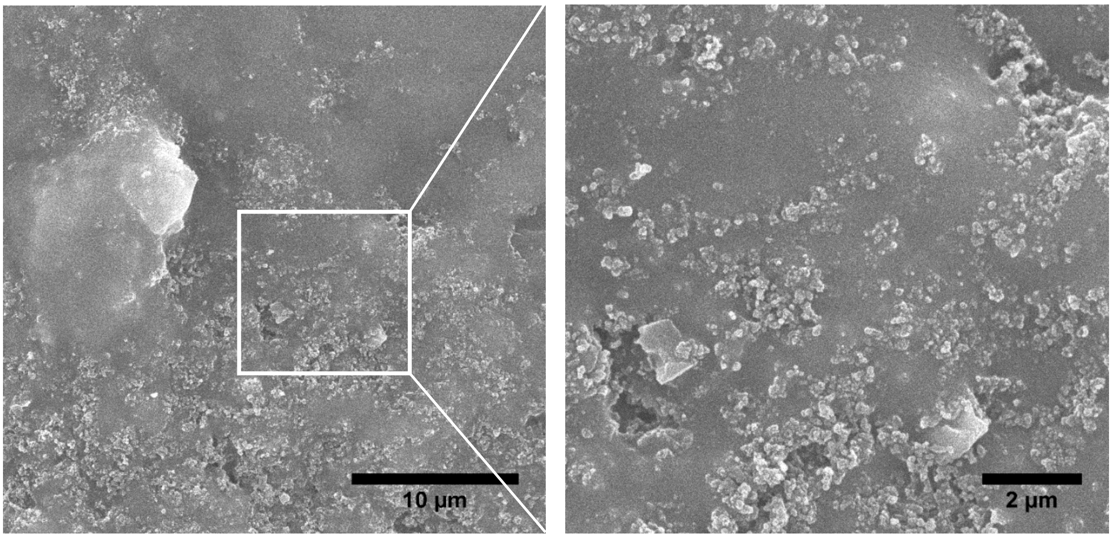

Figure 16. Scanning electronical microscope of composites surface structure after sintering； a) scale bar in 10 um; b) scale bar in 2 um.

The morphology of the GG/PTFE composite as printing is shown in SEM micrographs in Figure 13. SEM was taken for samples before and after high temperature thermal process uder the fabrication condition that give the most bulk PTFE Young's modulus similar properties. At low magnification (Figure 13 a), there is an abundance of evenly separated gellan gum fiber networks in un-sintered PTFE dispersion matrix, indicating good fiber network dispersion and distribution. At higher magnification (Figure 13 b, c, d), PTFE particles are well adhered and wetted along the fiber length. The PTFE particles with measured average diameters ~320nm preserve their round shape and do not appear significantly deformed. High magnification SEM of sintered composite (Figure 14 a, b) indicates two different structures from sintered material. As circled in the figure, internal structures and surface structures are identified and observed in higher magnification in the following figures (Figure 15, 16). In Figure 15, fibril-like structures from the inner part of the tensile specimen show interesting networking distribution. We raised one hypothesis that each fibril is composed by a series of PTFE particles wrapping along one gellan gum fiber during the sintering process. The measured average width of the fibril is around 540nm, which supports the hypothesis we concluded that the width is an add-up of PTFE particles wrapping on top of gellan gum fibers. Furthermore, the surface structure of sintered material is also investigated such that only round shape nodes are observed, as shown in Figure 16. An EDX was performed for sintered material to confirm the existence of fluorine elements as shown in Figure 17.

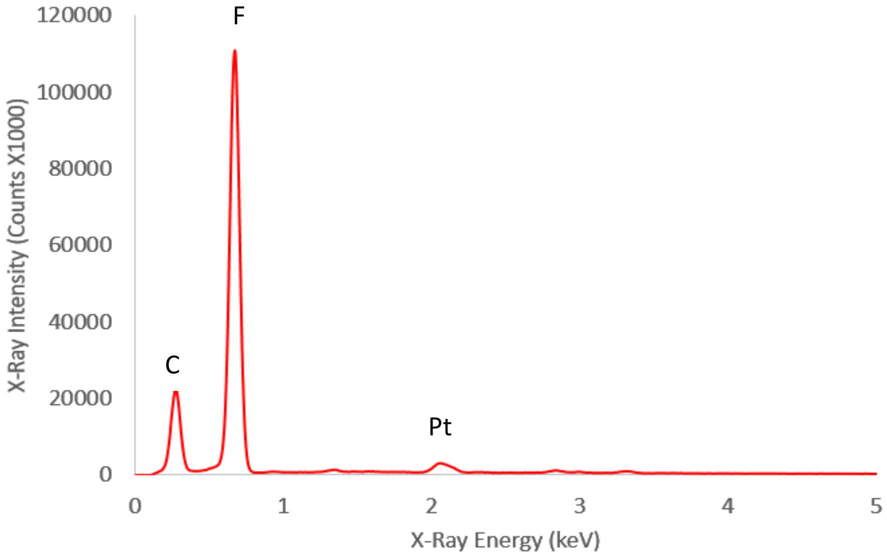

Figure 17. EDX of composites after sintering, indicating the existence of fluorine and carbon elements.

1.4 Conclusion

We successfully fabricated 3D structures of PTFE by adding gellan gum as binding materials with Direct Ink Writing 3D printing technique. Such material further went through various thermal process to obtain desirable mechanical properties. Morphology evidence show interesting networking structure of the matrix and binding materials. Further mechanical and optimization experiments under the Taguchi Design of Experiment will be performed and concluded in the next section.

2. Taguchi Design of Experiment of uniaxial tensile experiment for 3D printed PTFE structures

2.1 Introduction

2.1.1 Design of Experiment (DOE)

Design of experiment, or DOE, is the technique used for guiding the choice of the experiments to be performed in an efficient way. The data subject to experimental error or noise are usually involved, and the results can be significantly affected by error or noise. Appropriate statistical methods are therefore better to analyze the data. Replication, randomization, and blocking are three basic principles of statistical methods in experimental design.[52] More specifically, in order to obtain a more precise result with statistical errors, replication is defined as the repetition of the experiment. Randomization refers to the random order in which the runs of the experiment are to be performed.[53] In this way, the conditions in one run neither depend on the conditions of the previous run nor predict the conditions in the subsequent runs.[54] The sources of variability can be significantly reduced, and the precision is enhanced at the same time by arranging the experiments in groups that are similar to one another. Finally, numerical simulations will be used to replace runs of experiments, statistical issues are usually ignorable in this way. However, if one used it as a way of assessing the influence the noise factors will have in operation.[55]

2.1.2 Taguchi DOE

The quality of a product is one of the main factors which affects consumers' purchasing decision. Dr. Taguchi is one of the pioneers in filed of quality control and improvement, who advocated the use of experimental design. Reducing the variabilities around a final target is the core idea in Taguchi's philosophy. From Taguchi's point of view, there are three sequential stages for optimizing a product: system design, parameter design, and tolerance design.[56] The system design stage describes when new concepts or methods are introduced to a new product or process. Then the discussion of maintaining and improving the uniformity of products come out, and it was the parameter design stage. At this stage, the performance parameters of a product should be set to make the performance less sensitive to uncontrollable environmental conditions such as road temperature or humidity.[57] The range of variabilities are determined in the tolerance design stage. The activities at this stage may include selecting alternative raw materials or operation procedures. At the parameter design stage, Taguchi utilizes traditional method like ANOVA and orthogonal arrays with a new class of statistics called signal-to-noise ratios in designing an experiment. A standard L9 orthogonal array design is presented in Figure 18.

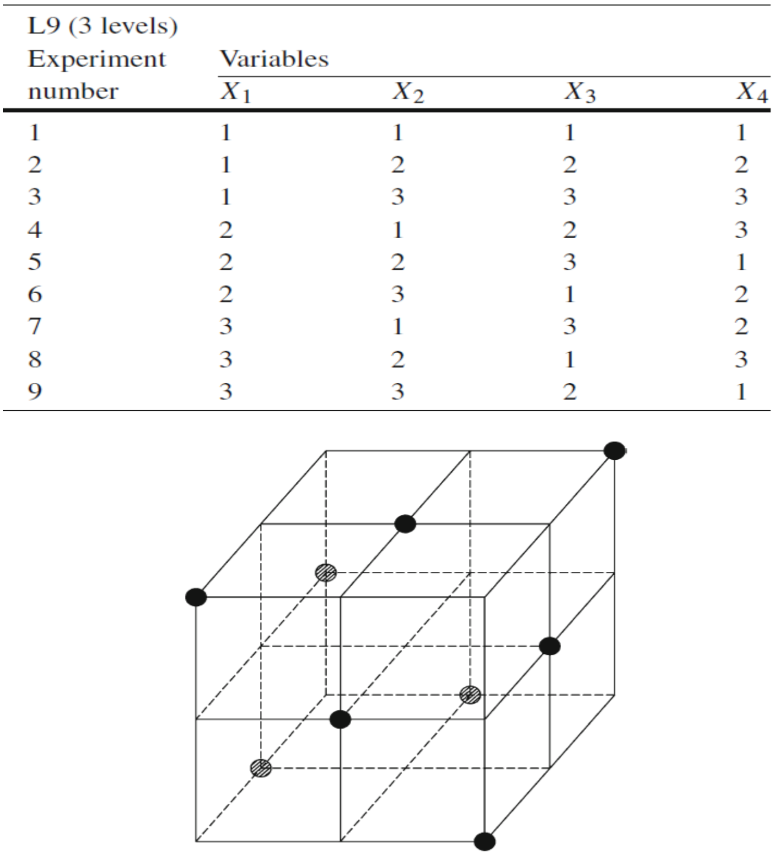

L9 (3 levels) Experiment number	Variables			
	X_1	X_2	X_3	X_4
1	1	1	1	1
2	1	2	2	2
3	1	3	3	3
4	2	1	2	3
5	2	2	3	1
6	2	3	1	2
7	3	1	3	2
8	3	2	1	3
9	3	3	2	1

Figure 18. L9 orthogonal array of Taguchi Design of Experiment.

2.2 Experimental Section

Micro-uniaxial tensile test: To impose uniaxial loading, the quasi-static model of Instron E-1000 was used with 0.02 s^{-1} strain rate under 200 N load cell. Tensile test specimens are made under ASTM 1708. The force-displacement responses reading from the machine were used to calculate the engineering stress-strain curves under each conditions.

2.3 Results and discussion

2.3.1 Taguchi DOE with three parameters in three levels

Levels of experimental factor	Gellan Gum weight percentage (%)	Maximum melting tempearture (°C)	Cooling rate (°C/hr)
1	0.5	340	12
2	1	380	60
3	1.5	420	150

Table 2. Three chosen parameters in three levels for Taguchi DOE.

L9	Gellan Gum Weight Percentage (%)	Tmax (°C)	Cooling rate (°C /hr)	Pattern
1	0.5	340	12	−−−
2	0.5	380	60	−00
3	0.5	420	150	−++
4	1.0	340	60	0−0
5	1.0	380	150	00+
6	1.0	420	12	0+−
7	1.5	340	150	+−+
8	1.5	380	12	+0−
9	1.5	420	60	++0

Table 3. Taguchi DOE L9 orthogonal array with three parameters in three levels.

Since one of the objective of this study is to select an optimal process parameter setting to yield a commercial PTFE similar 3D printed PTFE products, the design of experiments method was firstly implemented. Table 2 demonstrates three controllable three-level factors based on the printability and industrial standard as described in Figure 3. According to the printability results, one can identify three level of gellan gum weight percentage for investigation on its mechanical and surface properties. The sintering temperature and quenching rate are two other essential controllable factors for as printed structures. A desired L9 array with nine different patterns is created as indicators for experimental conditions. Table 3 lists the experimental conditions of the specimens for uniaxial tensile test and contact angle hydrophobicity test.

2.3.2 Uniaxial tensile test results under L9 Taguchi array

To impose uniaxial loading, the quasi-static model of Instron E-1000 was used with 0.02 s^{-1} strain rate under 200 N load cell. The force-displacement responses reading from the machine were used to calculate the engineering stress-strain curves under each conditions. Young's modulus calculation are based on the strain range from 0 to 0.5%. The tensile strength and tensile strain are calculated based on the ultimate point of stress-strain curve. The yield points of each curves are calculated based on 1% offset.

There controllable parameters with three levels require nine experimental conditions according to Taguchi DOE, twenty seven specimens were tested with three repeated runs per conditions. Results from three specimens under each condition show good consistency as shown in Figure 19-21. The averaged curves taking from all three samples under one condition are classified and demonstrated by the Gellan Gum weight percentage in Figure 19-21. The results were further analyzed by the analysis of variance (ANOVA) calculations to determine whether a given parameter is statistically significant as well as its percent contribution and main effect on the outcome. The following tables (Table 4-8) list out values extracting from Figure 19-21 with all twenty-seven samples. Means and Signal-to-Noise ratio are calculated and listed as well. The outcomes determined for uniaxial tensile loading case were predicated, and the ANOVA calculations were carried out to determine the effects.

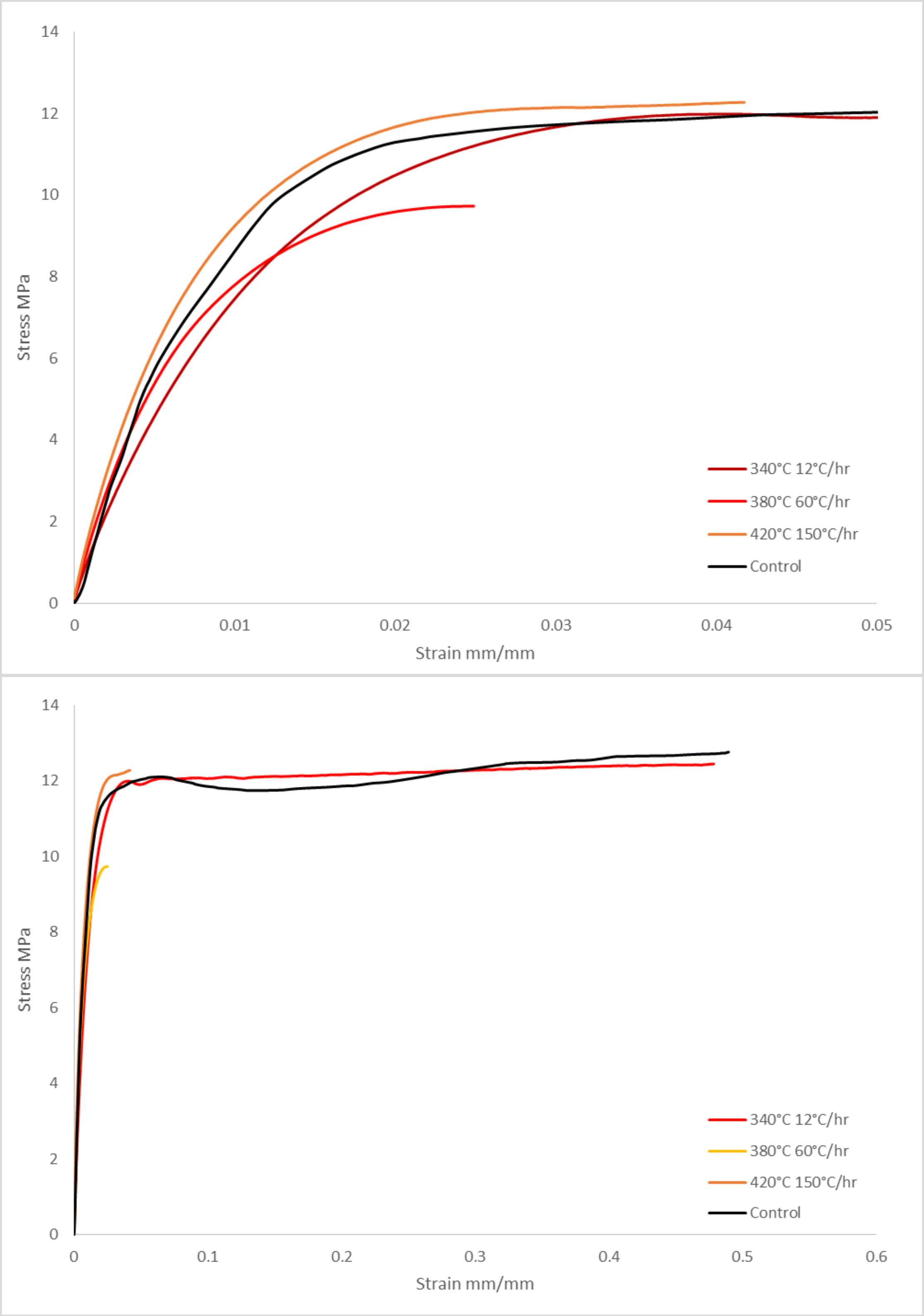

Figure 19. Engineering stress-strain curves of 0.5 wt% GG under three different combinations of thermal conditions; a) strain from range of 0 to 0.05; b) strain from range of 0 to 0.6

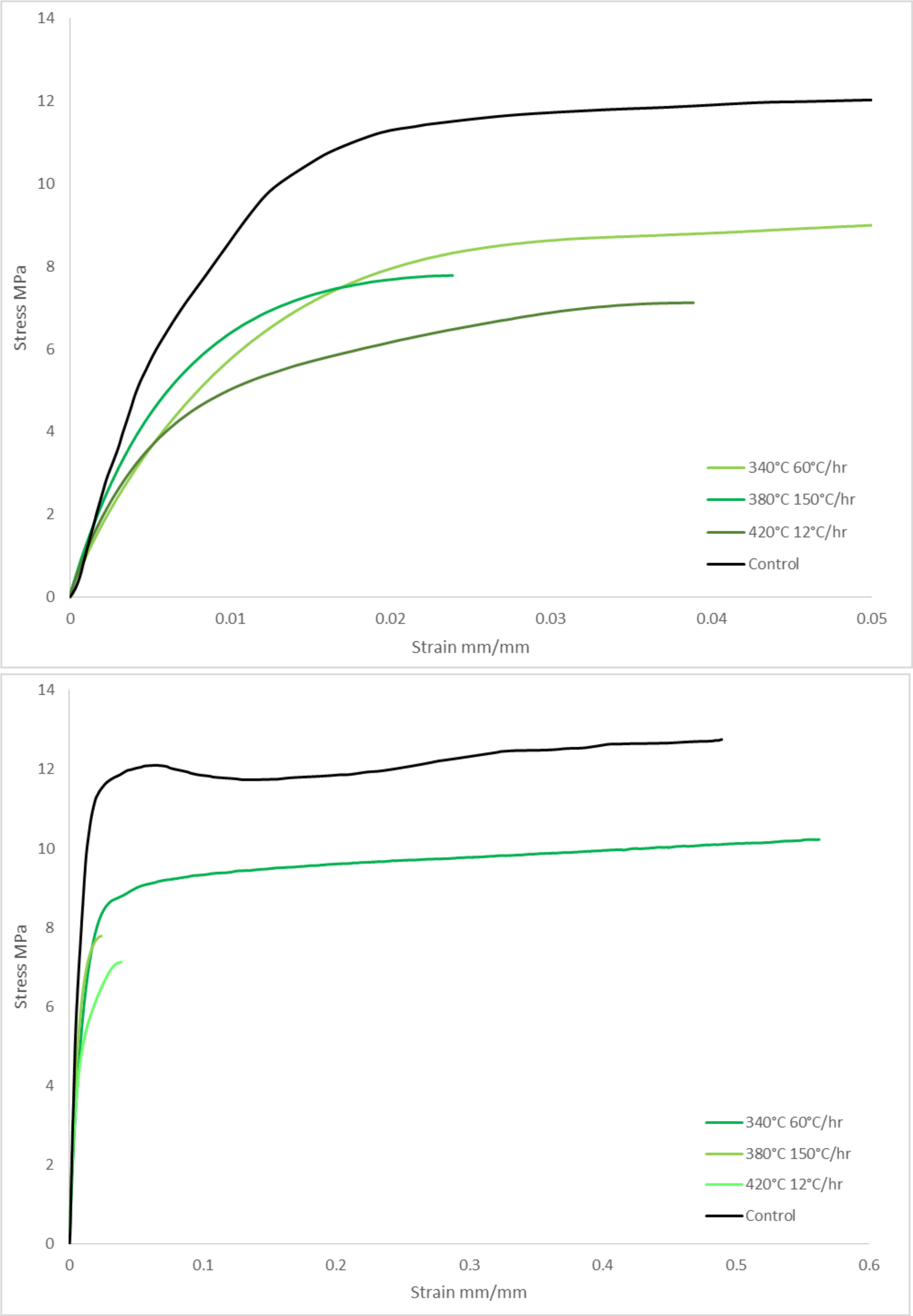

Figure 20. Engineering stress-strain curves of 1.0 wt% GG under three different combinations of thermal conditions; a) strain from range of 0 to 0.05; b) strain from range of 0 to 0.6

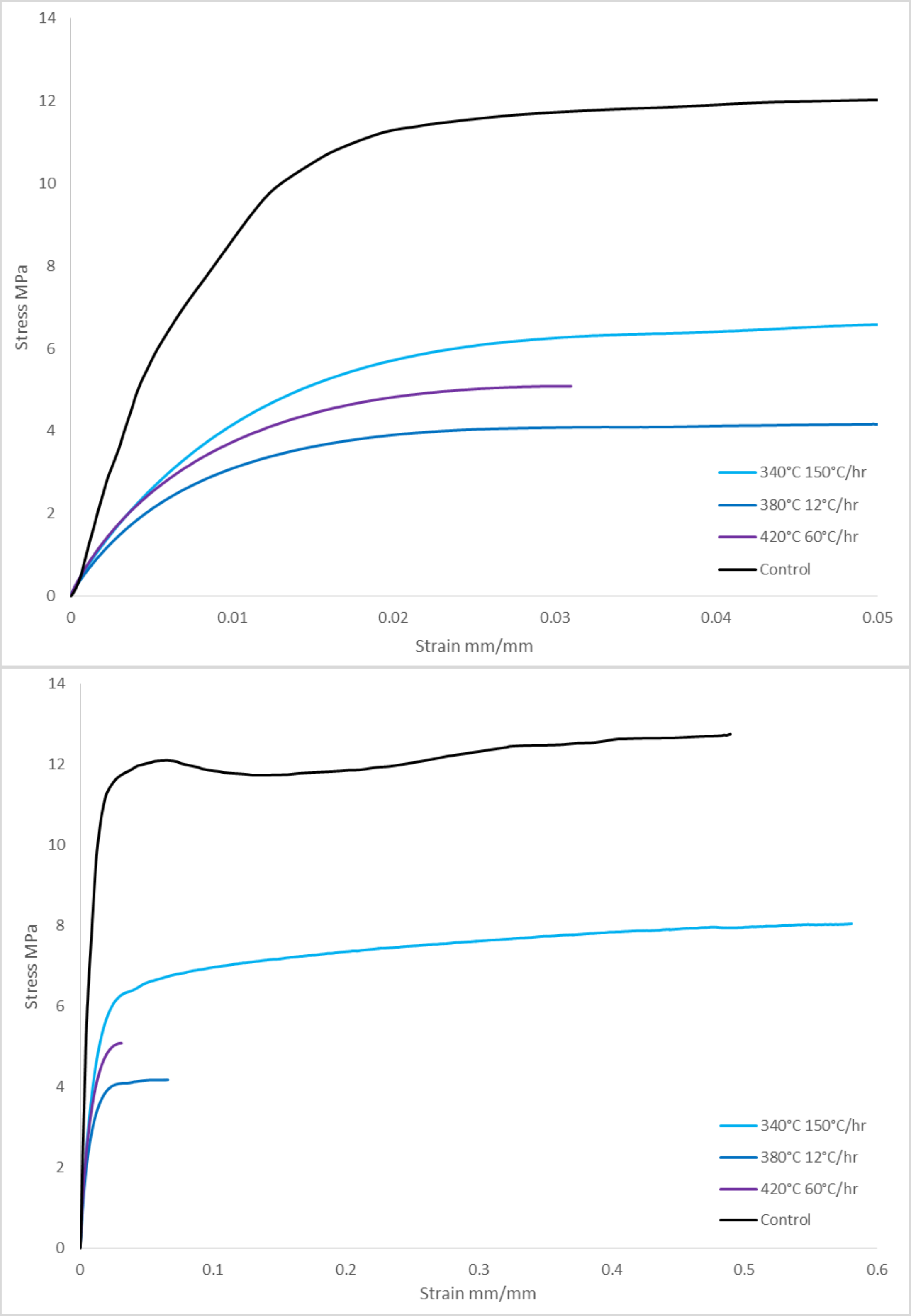

Figure 21. Engineering stress-strain curves of 1.5 wt% GG under three different combinations of thermal conditions; a) strain from range of 0 to 0.05; b) strain from range of 0 to 0.6

Young’s Modulus L9 Array	Sample 1 (MPa)	Sample 2 (MPa)	Sample 3 (MPa)	Mean (MPa)	S/N Ratio
1	840.70	947.02	933.85	940.70	59.47
2	1039.31	1216.54	1052.94	1102.92	60.79
3	1266.27	1237.11	1260.49	1254.62	61.97
4	745.83	752.35	706.95	735.05	57.32
5	954.38	897.29	882.37	911.35	59.18
6	765.28	826.15	794.23	795.22	57.99
7	533.72	517.66	505.63	508.31	54.11
8	467.53	438.48	400.53	435.51	52.73
9	466.89	496.45	564.49	509.28	54.06

Table 4. Measured Young’s modulus for defined Taguchi DOE L9 array.

1% offset Yield Strength L9 Array	Sample 1 (%)	Sample 2 (%)	Sample 3 (%)	Mean (%)	S/N Ratio
1	11.77	10.89	10.27	10.34	20.27
2	9.35	9.73	9.47	9.520	19.56
3	11.39	11.75	11.34	11.49	21.20
4	8.20	7.89	8.12	8.07	18.14
5	7.63	7.62	7.50	7.58	17.60
6	7.27	7.02	7.14	7.14	17.07
7	5.60	5.95	5.99	5.70	15.09
8	3.97	3.94	3.80	3.90	11.83
9	4.66	4.96	4.79	4.81	13.63

Table 5. Measured 1% offset Yield Strength for defined Taguchi DOE L9 array.

Tensile Strength L9 Array	Sample 1 (MPa)	Sample 2 (MPa)	Sample 3 (MPa)	Mean (MPa)	S/N Ratio
1	13.73	12.18	11.72	11.62	21.28
2	10.36	9.89	9.61	9.95	19.95
3	12.36	12.62	12.01	12.33	21.82
4	10.51	10.47	10.38	10.45	20.38
5	7.68	7.94	7.79	7.80	17.84
6	10.95	7.81	7.43	8.73	18.45
7	7.72	8.05	8.66	7.91	17.89
8	4.45	4.03	4.09	4.19	12.42
9	4.851	5.37	5.14	5.12	14.17

Table 6. Measured Tensile Strength for defined Taguchi DOE L9 array.

Ultimate Strain L9 Array	Sample 1 (%)	Sample 2 (%)	Sample 3 (%)	Mean (%)	S/N Ratio
1	40.2	68.33	50.58	41.55	-20.13
2	5.48	2.39	2.53	34.72	-30.82
3	4.35	4.69	3.73	4.26	-27.52
4	77.63	72.43	60.16	70.07	-3.24
5	4.33	2.69	2.64	3.22	-30.47
6	3.26	5.06	2.52	3.62	-29.86
7	62.98	61.53	56.21	49.39	-7.68
8	5.65	5.29	8.27	6.41	-24.34
9	2.85	3.52	2.89	3.09	-30.33

Table 7. Measured Ultimate Strain for defined Taguchi DOE L9 array.

Young's Modulus Factors	**P value**	**Significance (P value < 0.005)**
GG%	0.0036	√
Tmax	0.0647	×
Cooling rate	0.0369	√
Yield Strength Factors	**P value**	**Significance (P value < 0.005)**
GG%	0.0037	√
Tmax	0.0674	×
Cooling rate	0.1007	×
Tensile Strength Factors	**P value**	**Significance (P value < 0.005)**
GG%	0.0085	√
Tmax	0.0286	√
Cooling rate	0.138	×
Tensile Strain Factors	**P value**	**Significance (P value < 0.005)**
GG%	0.6414	×
Tmax	0.0118	√
Cooling rate	0.7108	×

Table 8. P-values and significance analysis for each chose parameters in defined Taguchi DOE.

Table 8 shows the P-values and significance of three parameters to all investigated mechanical properties. For the Young's modulus outcome, all parameters chosen are found to be significant for the Young's modulus studied. However, only the gellan gum weight percentage is found to be significant to materials' yield strength. The tensile strength was found to be influenced by both the gellan gum weight percentage and maximum sintering temperature. Tensile strain is found to be only affected by the maximum sintering temperature. The actual experimental conditions are normalized to three levels, and the predicted outcome values of each levels are shown in the following figures.

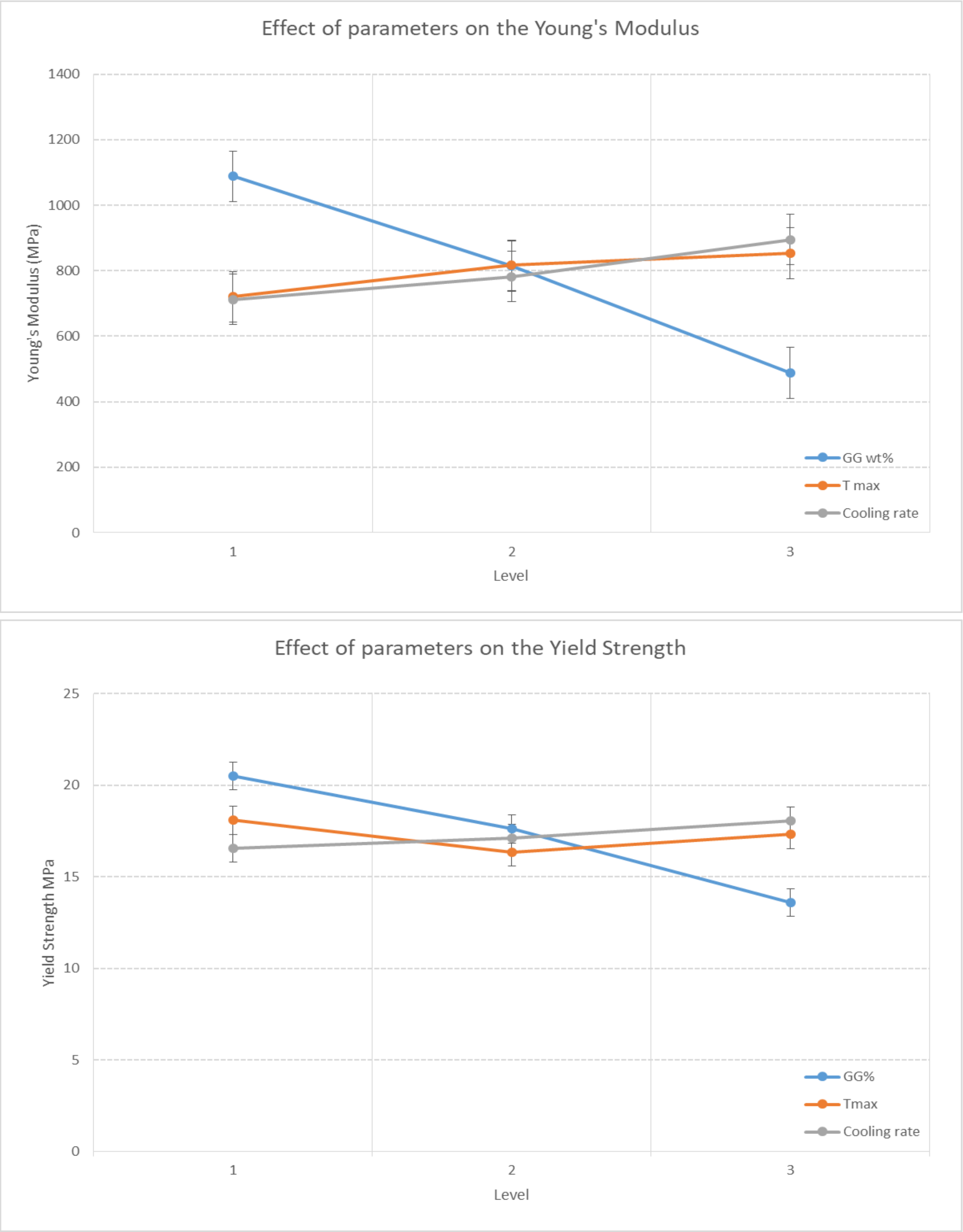

Figure 22. ANOVA on effects of chosen parameters on a) Young’s modulus, b) Yield strength.

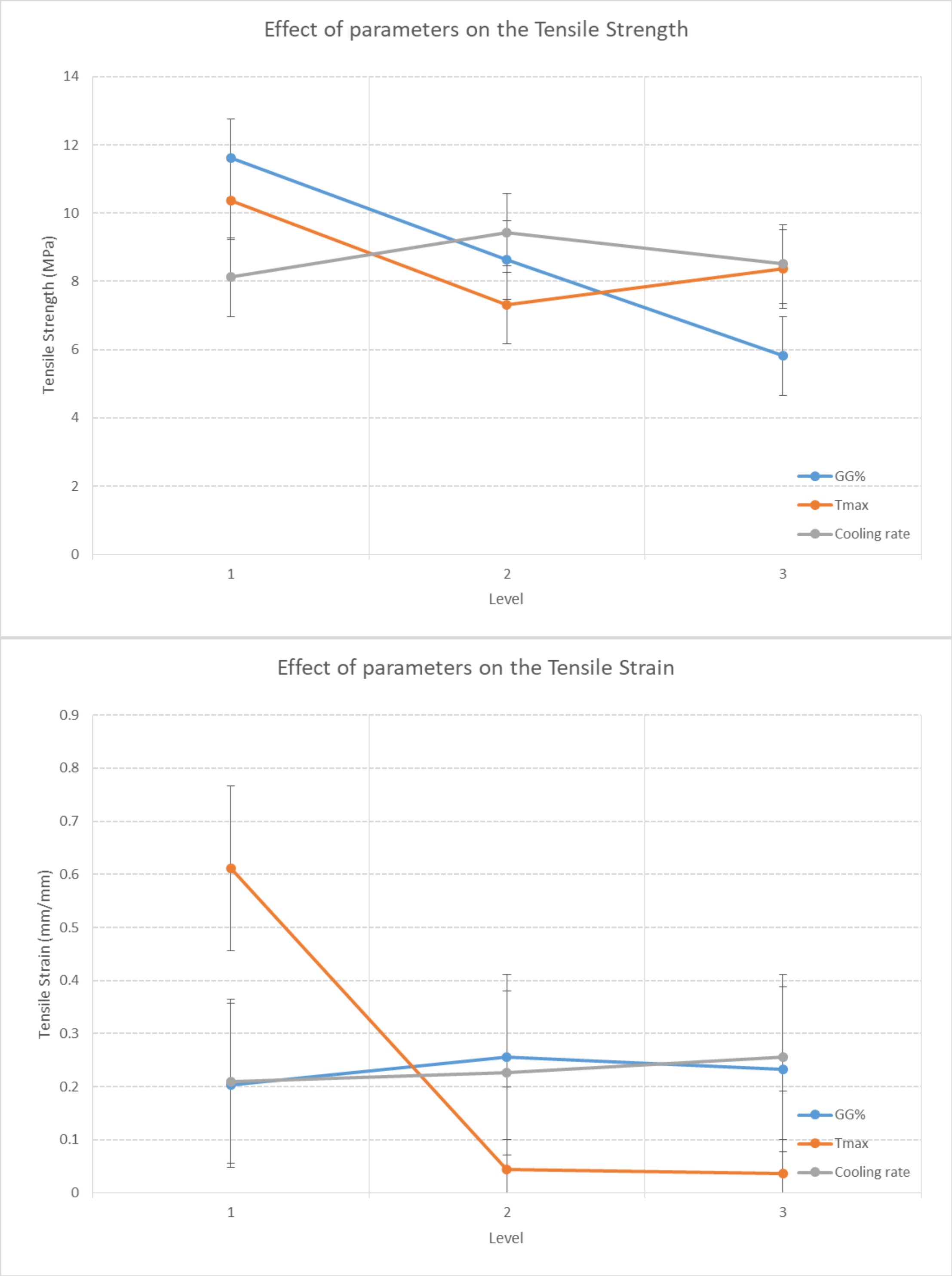

Figure 23. ANOVA on effects of chosen parameters on a) Tensile strength, b) Tensile strain.

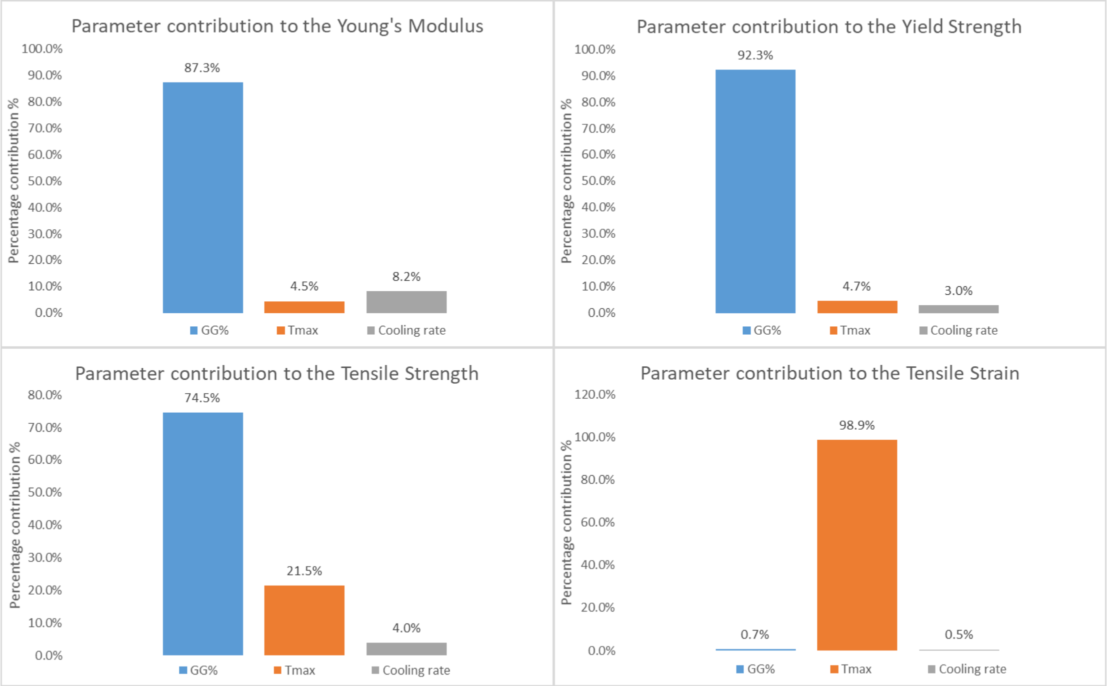

Figure 24. ANOVA on parameter contribution percentages on a) Young's modulus, b) Yield strength, c) Tensile strength, d) Tensile strain.

From Figure 22-24, effects on investigated mechanical properties of three chosen parameters are visualized and plotted in a normalized way. The contribution percentage and significance of material properties on the outcomes chosen are listed in Figure 24 as shown above. The gellan gum weight percentage in the composite has the highest contribution to the outcome with 89 out of 100 percentage, indicating it as the dominating effect over all three chosen factors as shown in Figure 22 a). The maximum temperature during sintering process and the cooling rate have similar contribution level to materials' Young's modulus. Higher percent contributions indicate higher influence on the outcome studied, where the maximum temperature and the cooling rate are believed to have small influence on both the Young's modulus and the yield strength. Moreover, Figure 22 b) shows the main effects of each parameters on the yield strength. The higher amount of gellan gum is used in the composite, the lower the yield strength the material will have. The maximum temperature shows a minimum yield strength in the middle level, while the cooling rate increase the yield strength as the levels increase. At the same time, these two factors have minimal effect on the Young's Modulus which are reflected with low percent contributions as shown in Figure 24 b).

Similarly, the effects and percentage contribution of the GG percentage, the maximum temperature and the cooling rate on both the tensile strength and tensile strain are analyzed and shown by ANOVA in Figure 23 and Figure 24 c) and d). The trend on tensile strength for the amount of gellan gum showing decreasing linearity, whereas the trend for the maximum temperature and cooling rate shows non-linear results. As for the tensile strain analysis, the maximum temperature is found to be the most influent factors out of the three with 98.9% contribution percentage. The rest of two factors, the Gellan Gum weight percentage and the cooling rate, are found to have low contribution percentage where shows in Figure 24 d) that less than 0.1 mm/mm strain change due to the level change of these two factors. At the same time, non-linear behaviors are found from the gellan gum weight percentage and the cooling rate for materials' tensile strain. This may explain by the degree of carbonization of the gellun gum fibers are affected by the sintering temperature where higher temperature burn away and vanish more amount of fibers.

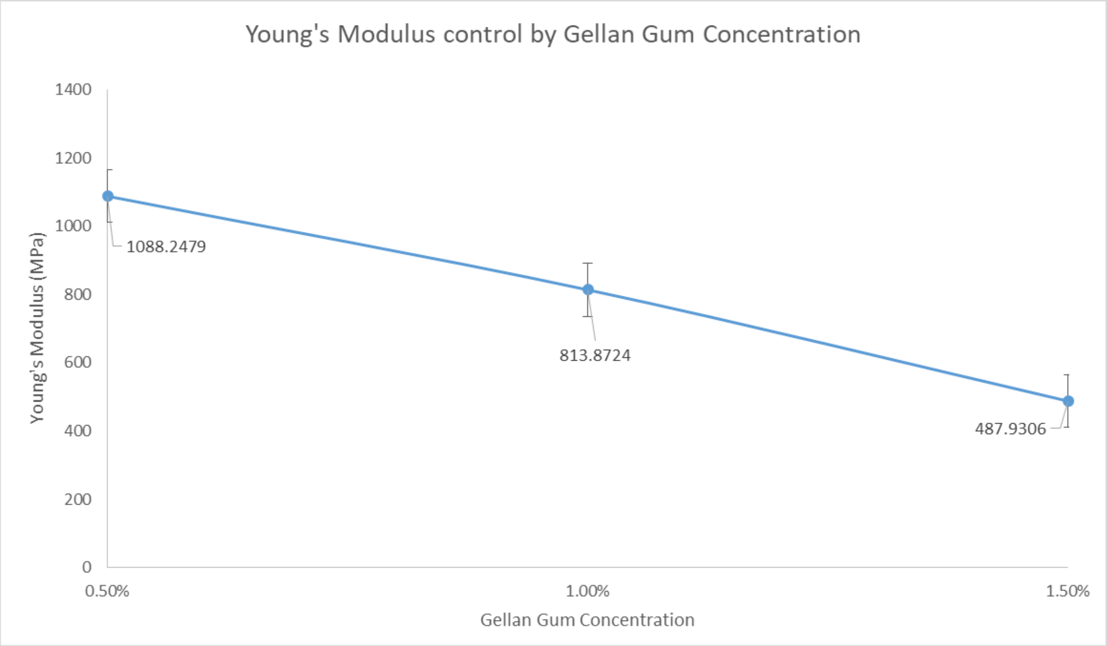

Figure 25. Tunability of the Young’s modulus by varying the gellan gum concentration.

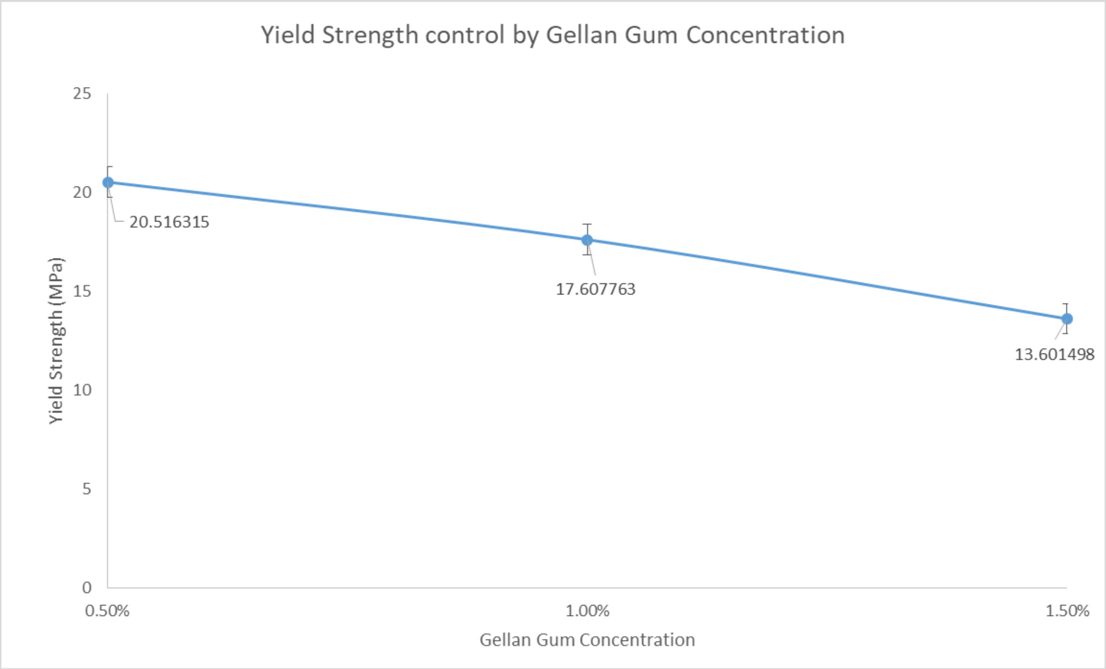

Figure 26. Tunability of the yield strength by varying the gellan gum concentration.

From Figure 25 and 26, the control of both Young's modulus and yield strength by three level of gellan gum weight percentage are presented. Both results show that the lowest amount of gellan gum is able to give the highest values of the Young's godulus and yield strength, which is consist with the ANOVA results. The error bar in both tunability results show good control of material properties. From literature[58-60], a typical range of the industrial fabricated bulk PTFE Young's modulus is from 471 to 1256 MPa depending on the tensile test rate. Typical bulk PTFE, testing under the same strain rate as our work, indicating the largest value of the range, 1256.32 MPa. As for the 1% offset yield strength, a typical range from 7.5 to 19.1 MPa is known. 10.30 MPa 1% offset yield strength is obtained under similar testing strain with our experiments. For printed PTFE materials, we tried to approach industrial fabricated bulk PTFE by matching material properties as much as possible. The comparison of both Young's modulus and yield strength between the best case scenarios predicted by the ANOVA results are shown in Table 9 and 10 as below. The effect and influence of the amount of gellan gum on the Young's modulus may be attributed to the core shell cylindrical structures. The gellan gum fibers, have low abilities to resist the strengthening force, were forming the core, and the crystallized PTFE particles wrapped around the core forming cylindrical shell that maintaining force resistance similar to solid PTFE materials. Hence, larger amount of gellan gum fibers as core structures results in a lower Young's modulus value. Finally, the engineering stress-strain curves tested under the highest and lowest Young's modulus fabrication conditions are compared with the engineering stress-strain curve of bulk PTFE as control.

	Predicted Young's Modulus (MPa)	Predicted Condition	Experimental Young's Modulus (MPa)
Literature Value	1240.89	N/A	N/A
Max Value	1245.45	0.5% 420° C 150° C/hr	1266.269
Min Value	337.75	1.5% 340° C 12° C/hr	339.29

Table 9. List of predicted values of the Young's modulus given by ANOVA and experimental values from uniaxial micro-tensile test. Literature values suggested bulk PTFE properties.

	Predicted Yield Strength (MPa)	Predicted Condition	Experimental Yield Strength (MPa)
Literature Value	10.30	N/A	N/A
Max Value	11.51	0.5% 420° C 150° C/hr	11.75
Min Value	3.70	1.5% 380° C 12° C/hr	3.81

Table 10. List of predicted values of yield strength given by ANOVA and experimental values from uniaxial micro-tensile test. Literature values suggested bulk PTFE properties.

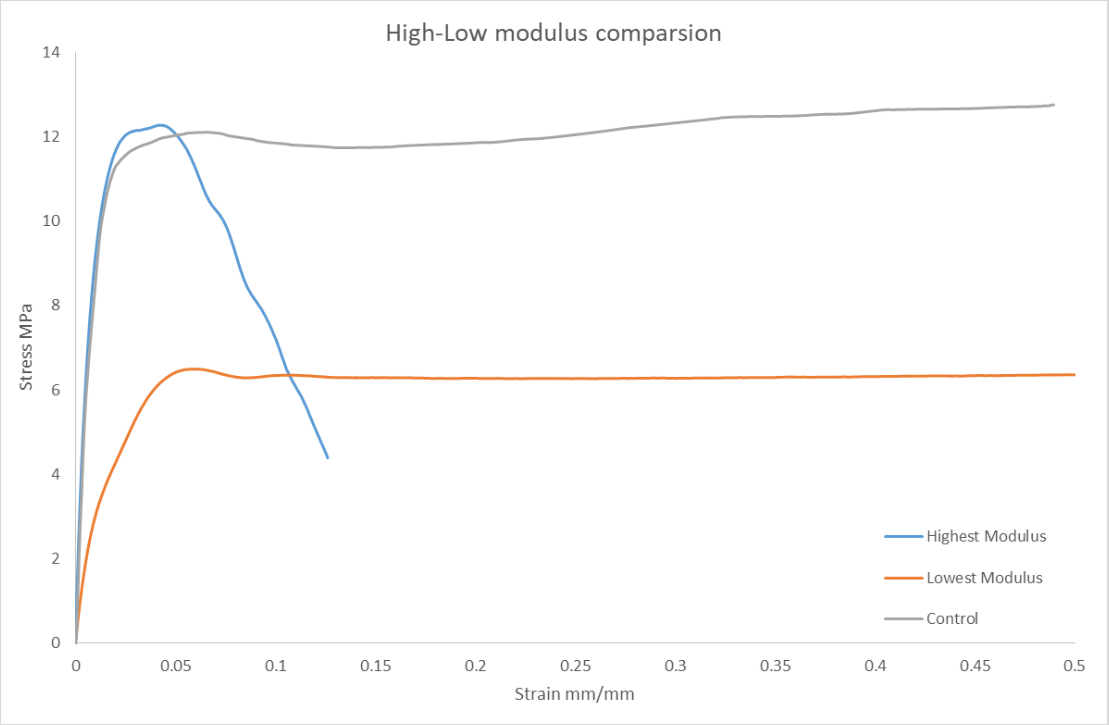

Figure 27. Comparison between the engineering stress-strain curves from the highest and lowest Young's modulus fabrication conditions to bulk PTFE control.

2.4 Conclusion

3D printable PTFE ink by DIW was first time made and printed to 3D structures with bulk PTFE similar mechanical properties including Young's modulus and yield strength. Furthermore, the Young's modulus and yield strength of such printed materials are tunable by varying the amount of binding material, gellan gum. Comparison between bulk PTFE mechanical properties and printed PTFE properties was made and listed. With Taguchi DOE, we identified the optimal thermal conditions for printed structures depending on one's need. This study paves the way for PTFE 3D printing where it is rarely developed.

Reference

1 Handbook, P. Teflon PTFE.

2 Moynihan, R. The Molecular Structure of Perfluorocarbon Polymers. Infrared Studies on Polytetrafluoroethylene1. *Journal of the American Chemical Society* **81**, 1045-1050 (1959).

3 Sperati, C. & McPherson, J. in *Proceedings of the Meeting of the American Chemical Society, Atlantiv City, NJ, USA.* 16-21.

4 Baker, J. L., Johnson, J. & Goldfarb, D. Expanded polytetrafluoroethylene (PTFE) subcutaneous arteriovenous conduit: an improved vascular access for chronic hemodialysis. *Transactions-American Society for Artificial Internal Organs* **22**, 382-387 (1976).

5 Blanchet, T. & Kennedy, F. Sliding wear mechanism of polytetrafluoroethylene (PTFE) and PTFE composites. *Wear* **153**, 229-243 (1992).

6 Feliciano, D. V., Mattox, K. L., Graham, J. M. & Bitondo, C. G. Five-year experience with PTFE grafts in vascular wounds. *The Journal of trauma* **25**, 71-82 (1985).

7 McCrum, N. An internal friction study of polytetrafluoroethylene. *Journal of Polymer Science* **34**, 355-369 (1959).

8 Książczak, A., Boniuk, H. & Cudziło, S. Thermal decomposition of PTFE in the presence of silicon, calcium silicide, ferrosilicon and iron. *Journal of thermal analysis and calorimetry* **74**, 569-574 (2003).

9 Bevers, D., Rogers, R. & Von Bradke, M. Examination of the influence of PTFE coating on the properties of carbon paper in polymer electrolyte fuel cells. *Journal of power sources* **63**, 193-201 (1996).

10 Wang, H., Zhao, J., Zhu, Y., Meng, Y. & Zhu, Y. The fabrication, nano/micro-structure, heat-and wear-resistance of the superhydrophobic PPS/PTFE composite coatings. *Journal of colloid and interface science* **402**, 253-258 (2013).

11 Giorgi, L., Antolini, E., Pozio, A. & Passalacqua, E. Influence of the PTFE content in the diffusion layer of low-Pt loading electrodes for polymer electrolyte fuel cells. *Electrochimica Acta* **43**, 3675-3680 (1998).

12 Zhu, S. J., Zhou, Y. Y., Takashi, O. & Wu, G. in *Materials Science Forum.* 827-830 (Trans Tech Publ).

13 Kanazawa, T., Matsuda, Y. & Tasaka, S. Fabrication of a porous structure of poly (tetrafluoroethylene) from a mixture with fumaric acid. *Polymer journal* **42**, 509 (2010).

14 Ebnesajjad, S. *Expanded PTFE Applications Handbook: Technology, Manufacturing and Applications*. (William Andrew, 2016).

15 Zhang, Y. *et al.* Fabrication and characterization of a PTFE-reinforced integral composite membrane for self-humidifying PEMFC. *Journal of power sources* **165**, 786-792 (2007).

16 Mouzakis, D. E. in *Lamination-Theory and Application* (InTech, 2018).

17 Lewis, J. A. & Gratson, G. M. Direct writing in three dimensions. *Materials today* **7**, 32-39 (2004).

18 Lewis, J. A. Direct ink writing of 3D functional materials. *Advanced Functional Materials* **16**, 2193-2204 (2006).

19 Cesarano, I. & Segalman, R. Robocasting provides moldless fabrication from slurry deposition. *Ceramic Industry* **148**, 94-100 (1998).

20 Cesarano III, J. & Calvert, P. US Patent 6 027 326, 2000. b) Q. Li, JA Lewis. *Adv. Mater* **15**, 1639 (2003).

21 Morissette, S. L., Lewis, J. A., Clem, P. G., Cesarano, J. & Dimos, D. B. Direct‐Write Fabrication of Pb (Nb, Zr, Ti) O3 Devices: Influence of Paste Rheology on Print Morphology and Component Properties. *Journal of the American Ceramic Society* **84**, 2462-2468 (2001).

22 Lous, G. M., Cornejo, I. A., McNulty, T. F., Safari, A. & Danforth, S. C. Fabrication of piezoelectric

ceramic/polymer composite transducers using fused deposition of ceramics. *Journal of the American Ceramic Society* **83**, 124-128 (2000).

23 Sachs, E., Cima, M., Williams, P., Brancazio, D. & Cornie, J. Three dimensional printing: rapid tooling and prototypes directly from a CAD model. *Journal of Engineering for Industry* **114**, 481-488 (1992).

24 Seerden, K. A. *et al.* Ink‐jet printing of wax‐based alumina suspensions. *Journal of the American Ceramic Society* **84**, 2514-2520 (2001).

25 Smay, J. E., Gratson, G. M., Shepherd, R. F., Cesarano III, J. & Lewis, J. A. Directed colloidal assembly of 3D periodic structures. *Advanced Materials* **14**, 1279-1283 (2002).

26 Hutmacher, D. W. *et al.* Mechanical properties and cell cultural response of polycaprolactone scaffolds designed and fabricated via fused deposition modeling. *Journal of biomedical materials research* **55**, 203-216 (2001).

27 Mott, M. & Evans, J. Zirconia/alumina functionally graded material made by ceramic ink jet printing. *Materials Science and Engineering: A* **271**, 344-352 (1999).

28 Therriault, D., Shepherd, R. F., White, S. R. & Lewis, J. A. Fugitive inks for direct‐write assembly of three‐dimensional microvascular networks. *Advanced Materials* **17**, 395-399 (2005).

29 Gratson, G. M. & Lewis, J. A. Phase behavior and rheological properties of polyelectrolyte inks for direct-write assembly. *Langmuir* **21**, 457-464 (2005).

30 Therriault, D., White, S. R. & Lewis, J. A. Chaotic mixing in three-dimensional microvascular networks fabricated by direct-write assembly. *Nature materials* **2**, 265 (2003).

31 Hutmacher, D. W. *et al.* Mechanical properties and cell cultural response of polycaprolactone scaffolds designed and fabricated via fused deposition modeling. *Journal of Biomedical Materials Research: An Official Journal of The Society for Biomaterials, The Japanese Society for Biomaterials, and The Australian Society for Biomaterials and the Korean Society for Biomaterials* **55**, 203-216 (2001).

32 Xu, M., Gratson, G. M., Duoss, E. B., Shepherd, R. F. & Lewis, J. A. Biomimetic silicification of 3D polyamine-rich scaffolds assembled by direct ink writing. *Soft Matter* **2**, 205-209 (2006).

33 Smay, J. E., Cesarano III, J., Tuttle, B. A. & Lewis, J. A. Piezoelectric properties of 3-X periodic Pb (Zr x Ti 1− x) O 3–polymer composites. *Journal of Applied Physics* **92**, 6119-6127 (2002).

34 Gratson, G. M. *et al.* Direct‐write assembly of three‐dimensional photonic crystals: conversion of polymer scaffolds to silicon hollow‐woodpile structures. *Advanced Materials* **18**, 461-465 (2006).

35 Milas, M., Shi, X. & Rinaudo, M. On the physicochemical properties of gellan gum. *Biopolymers: Original Research on Biomolecules* **30**, 451-464 (1990).

36 Ogawa, E. in *Physical Chemistry and Industrial Application of Gellan Gum* 8-14 (Springer, 1999).

37 Crescenzi, V. & Dentini, M. The influence of side-chains on the dilute-solution properties of three structurally related, bacterial anionic polysaccharides. *Carbohydrate research* **160**, 283-302 (1987).

38 Nishinari, K., Miyoshi, E., Takaya, T. & Williams, P. A. Rheological and DSC studies on the interaction between gellan gum and konjac glucomannan. *Carbohydrate Polymers* **30**, 193-207 (1996).

39 Ogawa, E. Conformational properties of polysaccharide gellan gum in aqueous solutions. *Recent Research Developments in Macromolecular Research* **2**, 81-94 (1997).

40 Miyoshi, E., Takaya, T. & Nishinari, K. Rheological and thermal studies of gel-sol transition in gellan gum aqueous solutions. *Carbohydrate Polymers* **30**, 109-119 (1996).

41 Thu, B. *et al.* Alginate polycation microcapsules: I. Interaction between alginate and polycation. *Biomaterials* **17**, 1031-1040 (1996).

42 Rinaudo, M. & Milas, M. in *Developments in Food Science* Vol. 41 239-263 (Elsevier, 2000).

43 Grasdalen, H. & Smidsrød, O. Gelation of gellan gum. *Carbohydrate polymers* **7**, 371-393 (1987).

44 Morris, V. J. *et al.* Atomic force microscopy as a tool for interpreting the rheology of food biopolymers at the molecular level. *LWT-Food Science and Technology* **34**, 3-10 (2001).

45 Carroll, V., Miles, M. & Morris, V. Fibre-diffraction studies of the extracellular polysaccharide from Pseudomonas elodea. *International Journal of Biological Macromolecules* **4**, 432-433 (1982).

46 Chandrasekaran, R. & Thailambal, V. The influence of calcium ions, acetate and L-glycerate groups on the gellan double-helix. *Carbohydrate Polymers* **12**, 431-442 (1990).

47 Kuo, M.-S., Mort, A. J. & Dell, A. Identification and location of L-glycerate, an unusual acyl substituent in gellan gum. *Carbohydrate Research* **156**, 173-187 (1986).

48 Shinyashiki, N., Sakai, T., Yamada, G. & Yagihara, S. in *Physical Chemistry and Industrial Application of Gellan Gum* 36-40 (Springer, 1999).

49 O'Neill, M. A., Selvendran, R. R. & Morris, V. J. Structure of the acidic extracellular gelling polysaccharide produced by Pseudomonas elodea. *Carbohydrate Research* **124**, 123-133 (1983).

50 Miyoshi, E. & Nishinari, K. in *Physical Chemistry and Industrial Application of Gellan Gum* 68-82 (Springer, 1999).

51 Tanaka, Y., Sakurai, M. & Nakamura, K. Ultrasonic velocity and circular dichroism in aqueous gellan solutions. *Food hydrocolloids* **10**, 133-136 (1996).

52 Cavazzuti, M. in *Optimization Methods* 13-42 (Springer, 2013).

53 Cavazzuti, M. *et al.* Structural Optimization of Automotive Chassis: Theory, Setup, Design. *Structural and Multidisciplinary Optimization*, 1-3 (2011).

54 Cavazzuti, M. *et al.* High performance automotive chassis design: a topology optimization based approach. *Structural and Multidisciplinary Optimization* **44**, 45-56 (2011).

55 Park, G.-J. Design of experiments. *Analytic Methods for Design Practice*, 309-391 (2007).

56 Taguchi, G., Konishi, S. & Konishi, S. *Taguchi Methods: Orthogonal Arrays and Linear Graphs. Tools for Quality Engineering*. (American Supplier Institute Dearborn, MI, 1987).

57 Taguchi, G. Taguchi on Robust Technology Development: Bringing Quality Engineering Upstream (Asme Press Series on International Advances in Design Productivity). (1993).

58 Rae, P. & Dattelbaum, D. The properties of poly (tetrafluoroethylene)(PTFE) in compression. *Polymer* **45**, 7615-7625 (2004).

59 Ansari, M., Vavlekas, D., McCoy, J. & Hatzikiriakos, S. Paste extrusion and mechanical properties of PTFE. *International Polymer Processing* **30**, 603-614 (2015).

60 Joyce, J. A. Fracture toughness evaluation of polytetrafluoroethylene. *Polymer Engineering & Science* **43**, 1702-1714 (2003).

Curriculum Vitae

Danny (Zhuoran) Jiang

EDUCATION

University of Oxford – Oxford, UK starting October 2018

Doctor of Philosophy, Department of Engineering Sciences/The Institute of Biomedical Engineering

Johns Hopkins University – Baltimore, USA anticipated July 2018

Master of Science, Department of Chemical and Biomolecular Engineering

Thesis: *3D Printing PTFE with Direct Ink Writting*

McGill University – Montreal, Canada June 2016

Bachelor of Engineering, Department of Chemical Engineering

PROFESSIONAL EXPERIENCE

Graduate Research Assistant, Dept. of ChemBE, Johns Hopkins University, USA 2016-2018

Invented pioneering 3D printable Teflon composite leading to various customizable biomedical implants and devices fabrication, as well as two scientific journal paper publication that one listed as the first author and the other one listed as the co-first author for soft material 4D printing.

Undergraduate Research Assistant, Dept. of ChemE, McGill University, Canada 2015-2016

Experimented on a novel nanomaterial system and implemented its environmental application in water pollution, resulting into one scientific journal paper publication listed as the second author, one invited presentation on an international conference and one awarded undergraduate poster presentation session.

Undergraduate Student Consultant, Hatch Consulting Firm, Canada 2015-2016

Performed a complete feasibility report for an unimplemented stainless steel making process with innovated technologies as undergraduate senior design project under supervised by senior consultants to guide stainless steel factories in mainly technical, environmental and financial decisions makings.

AWARDS AND HONORS

Johns Hopkins University ChemBE Master's Essay-Based Track Scholarship Award	2017-2018
Brain Hirst Undergraduate Research in Engineering Award in Sustainable Engineering	2015
McGill University International Entrance Award	2013

PUBLICATIONS

- Jiang, Z., Chatterje, D., Erol, O., Kang, S.H. & Gracias, D. 3D printing of PTFE with Direct Ink Writing. *In preparation.*
- Khan, H., Jiang, Z., & Berk, D. (2018). Molybdenum doped graphene/TiO 2 hybrid photocatalyst for UV/visible photocatalytic applications. *Solar Energy*, 162, 420-430.
- Bei, K., Wang, J.,.. Jiang, Z.,.. & Pan, Z. (2018). Determining the volume expansion of the CO 2+ octane mixture using a fused silica capillary cell with in-situ Raman spectroscopy. *Journal of CO2 Utilization*, 24, 149-156.